FOALAB

Dept. of Earth Sciences, University of Oxford

Summer Project

"Generalised stability theory in magma/mantle dynamics"

Author:
Owen Evans

Supervisors:
Dr. Richard Katz, Dr. Sander Rhebergen

September 12th, 2013

Contents

1 Introduction

Within the earth, locations where liquid magma and partially molten mantle co-exist together, are hotbeds for important geophysical phenomena. The dynamics at these locations are

therefore of critical importance to understanding and answering fundamental questions about the Earth.

Modeling this two-phase interaction is a problem that concerns fluid dynamicists: such processes can be described by the flow of a low-viscosity fluid in a viscously deformable, permeable matrix [18]. Within the framework of continuum mechanics, a system of conservation equations were developed to extend the mantle convection equations to include magmatism (McKenzie 1984 [11]; Scott and Stevenson 1986 [17]). A brief derivation of these equations are described in the next section. The resulting system is highly non-linear, and therefore impossible to solve exactly. There are, however, both analytical and computational approaches to overcoming its intractability. One approach to studying the equations in [11] involves numerical methods, and the use software packages to provide simulations. The development of advanced numerical software that can utilise both linear and nonlinear solvers in a higly parallel manner has helped to realise this. Other approaches to analysing such nonlinear systems date back to work done by 19th century mathematicians, which determine the stability of a system of PDEs. This "stability" anaylsis involves the linearisation of the system about some known time-independent base-state solution, and characterising the trajectories of small perturbations to this base-state. Understanding the growth of small perturbations to the system in question is a useful, powerful approach (Spiegelman 2003 [19]; Katz 2006 [7].)

Although traditional stability analysis can be useful for studying nonlinear systems, it only takes into account the asymptotic stability. This doesn't provide information regarding transient perturbations that the system may experience, over a finite time window. This occurs when the linearised system is non-normal; that is, its eigenfunctions are not orthogonal. Identifying transient deviations over finite time can be significant for understanding the complete behaviour of a physical system, which has motivated the development of a "generalised" stability theory. We make use a new software library, created as part of the dolfin-adjoint project [13], which automates the generalised stability theory calculations in conjunction with the FEniCS system. In the context of magma/mantle dynamics, the motivation is to use generalised stability theory as a tool that can complement and advance existing studies, and motivate new experiments. This report presents a preliminary study.

2 Governing Equations

We begin with a review of the two-phase model, based on the formulation taken in [11]. This exposition is based on averaging field values over a "representative volume element" (RVE) of the two-phase mixture. Microscopically, mechanical fields tend to be higly heterogeneous, due to the drastic changes between phases. This microscopic heterogeneity is dealt with by averaging over the RVE, which represents a continuum of field values at the macroscopic scale, yet contains a sufficient proportion of grains and pores at the microscopic scale.

As we will be interested in integrating scalar quantities within the RVE, we first observe that for a general conserved scalar quantity ψ:

$$\frac{d}{dt}\int_{RVE}\psi \mathrm{d}V = -\int_{\partial RVE}\psi \mathbf{v}\cdot \mathrm{d}\mathbf{S} + \int_{RVE}\Omega \mathrm{d}V. \tag{1}$$

This says that the rate of change of the amount of ψ in the RVE is equal to the net flux of

ψ across the boundary plus the rate at which ψ is produce by a source(s) within the RVE. Here $\mathbf{v}$ is the material velocity and Ω is the volumetric production rate of ψ.

We restrict the RVE to containing only two phases; that is, the liquid magma and solid mantle. We define the porosity ϕ to be the volume fraction of liquid within the RVE. In turn, this means that $1-\phi$ will be the volume fraction of solid.

2.1 Conservation of mass

We define ρ_f and ρ_m to be the respective densities of the liquid and solid phases. It is assumed that these quantities are constant within the RVE. We can now write the respective masses of the liquid and solid as $\rho_f\phi$ and $\rho_m\phi$. Substituting $\rho_f\phi$ into (1) gives an equation for the conservation of liquid mass:

$$\frac{d}{dt}\int_{RVE}\rho_f\phi \mathrm{d}V = -\int_{\partial RVE}\rho_f\phi\mathbf{v}_f\cdot\mathrm{d}\mathbf{S} + \int_{RVE}\Gamma\mathrm{d}V, \tag{2}$$

where Γ is defined to be the melting rate. To rewrite this we can bring the derivative inside the first integral (as the volume element is considered to be fixed), and apply the divergence theorem to the second term to get (after some rearrangement):

$$\int_{RVE}(\frac{\partial(\rho_f\phi)}{\partial t} + \nabla\cdot\rho_f\phi\mathbf{v}_f)\mathrm{d}V = \int_{RVE}\Gamma\mathrm{d}V. \tag{3}$$

Equation (3) is true for an arbitrary volume, therefore the relationship holds for any point in space, and the integral signs can be neglected. Hence we have that

$$\frac{\partial(\rho_f\phi)}{\partial t} + \nabla\cdot\rho_f\phi\mathbf{v}_f = \Gamma. \tag{4}$$

Applying an identical argument to the solid phase gives the equation for the conservation of solid mass as

$$\frac{\partial\rho_m(1-\phi)}{\partial t} + \nabla\cdot\rho_m(1-\phi)\mathbf{v}_m = -\Gamma \tag{5}$$

2.2 Conservation of momentum

We now require two further equations that are statements of conservation of momentum for both the solid and liquid phases. Unlike the derivation of the conservation mass equation for a single phase, an additional force that accounts for the interaction between the two phases must be included. Physically, this "interphase" force is a result of the relative movement of the matrix and melt, and we define $\mathbf{I}$ to be the force on the matrix caused by the motion of the liquid. In order to obtain the conservation of momentum equation for the matrix we first invoke Newton's second law. An additional term is included, that accounts for the momentum flux out of the RVE, as we are considering a "fixed" volume. This means that momentum

can flow in or out by advection. The statement of conservation of momentum for the matrix phase can therefore be written as

$$\frac{d}{dt}\int_{RVE}\rho_m(1-\phi)\mathbf{v}_m \mathrm{d}V = -\int_{\partial RVE}\rho_m(1-\phi)\mathbf{v}_m\mathbf{v}_m\cdot\mathrm{d}\mathbf{S}+\int_{RVE}\mathbf{I}\mathrm{d}V + \int_{\partial RVE}(1-\phi)\sigma^m\cdot\mathrm{d}\mathbf{S}+\int_{RVE}\rho_m(1-\phi)\mathbf{g}\mathrm{d}V. \quad (6)$$

Here $\mathbf{g}$ is the acceleration due to gravity and $\sigma^{\mathbf{m}}$ is the stress tensor acting on the solid phase. As is discussed in [11], the Reynolds number for flows of physical relevance is very small ($\sim 10^{-8}$) for the melt, and even smaller for the matrix (assuming that the porosity is sufficiently small), which allows us to neglect the momentum term on the LHS of equation (6). It is also assumed that the rate of change of momentum is small. This assumption allows the first term on the LHS to be neglected, so that equation (6) becomes a statement of force balance. Applying the divergence theorem and dropping the integrals in a similar manner as before gives

$$-g(1-\phi)\delta_{i3}+I_i+\frac{\partial(\sigma^m_{ij}(1-\phi))}{\partial x_j}=0, \quad (7)$$

where the summation convention has been adopted, with i taking values 1, 2 and 3. The minus sign in front of the first term comes from the fact that we have selected the z-direction such that $\mathbf{g}\cdot\hat{\mathbf{k}}=-g$.

A similar approach is used to obtain the momentum equation for the liquid phase. Consideration of Newton's third law, however, means that the sign of the interphase force should be flipped (ie. there is an equal and opposite force of the matrix phase on the liquid phase.) This gives us that

$$-\phi g\delta_{i3}-I_i+\frac{\partial(\sigma^f_{ij}\phi)}{\partial x_j}=0, \quad (8)$$

where the stress tensor within the liquid is denoted by σ^f_{ij}. The next step is to properly define what the interphase and stress tensors are, and then substitute these definitions in equations (7) and (8).

The interphase force should not depend on the frame used to measure the velocities. Despite having a number of choices that posses this property, we will choose the relative velocity of the liquid with respect to the matrix phase, given by $\mathbf{v}_f-\mathbf{v}_m$. We also take for granted that the interphase force must include a fluid pressure term, due to a force that is a result of a gradient in the porosity. We write the interphase force as

$$\mathbf{I}=C_1(\mathbf{v}_f-\mathbf{v}_m)-P_f\nabla\phi. \quad (9)$$

A number of other terms could be included here, however the inclusion of such terms means that we would no longer have something that satisfies D'Arcy's law. In this equation we have that C_1 is a constant and P_f is the pressure in the melt. The stress tensor is taken to be in the form as expressed for an incompressible fluid:

$$\sigma_{ij}=-p\delta_{ij}+\mu(\frac{\partial v_i}{\partial x_j}+\frac{\partial v_j}{\partial x_i}). \quad (10)$$

The first term accounts for normal stresses and the second for viscous stresses (μ is the dynamic viscosity). As we are averaging over a RVE, we assume that there is sufficient self-cancellation of the second term to neglect it entirely. We then take $p = P_f$ and

$$C_1 = \mu\phi^2/K, \tag{11}$$

where μ is considered to be constant, and K is the permeability of the matrix, with the assumption that $K = K(\phi)$. Substitution of (9) and (10) into (8) gives the force balance law for the fluid:

$$\phi(\mathbf{v}_f - \mathbf{v}_m) = -\frac{K}{\mu}\nabla(P_f + \rho_f g z). \tag{12}$$

This equation tells us that segregation of magma from the porous matrix is driven by pressure gradients and body forces in the fluid.

At this point we turn our attention to the conservation of momentum equation for the solid phase, which we treat as a compressible, highly viscous fluid. For a compressible fluid, the general form of the stress tensor is given by

$$\sigma_{ij} = -p\delta_{ij} + \xi\delta_{ij}\frac{\partial v_k}{\partial x_k} + \eta\left(\frac{\partial v_i}{\partial x_j} + \frac{\partial v_j}{\partial x_i} - \frac{2}{3}\delta_{ij}\frac{\partial v_k}{\partial x_k}\right). \tag{13}$$

Substituting $p = P_f$ and $\mathbf{v} = \mathbf{v}_m$ gives the stress tensor for the matrix as

$$\sigma_{ij} = -P_f\delta_{ij} + \xi\delta_{ij}\frac{\partial v_k^m}{\partial x_k} + \eta\left(\frac{\partial v_i^m}{\partial x_j} + \frac{\partial v_j^m}{\partial x_i} - \frac{2}{3}\delta_{ij}\frac{\partial v_k^m}{\partial x_k}\right). \tag{14}$$

We define the matrix pressure to be $-\frac{1}{3}$ of the trace of the solid stress tensor. Using (14) we compute the matrix pressure to be

$$\begin{aligned} P_m &= -\frac{1}{3}\left[-3P_f + 3\xi\frac{\partial v_k^m}{\partial x_k} + \eta\left(2\frac{\partial v_i^m}{\partial x_i} - 2\frac{\partial v_k^m}{\partial x_k}\right)\right], \\ &= P_f - \xi\nabla\cdot\mathbf{v}_m. \end{aligned}$$

Here ξ is the bulk viscosity, which can be a function of temperature, porosity or other variables. This relationship is considered to be the simplest between the σ_{ij} and $\mathbf{v}_m$ that describes the flow and is valid for low stresses. The assumption of small stresses permits the assumption of linear shear stress terms in equation (14).

We define $\mathcal{C} = \nabla\cdot\mathbf{v}_m$ to be the "compaction rate" (or "isotropic strain rate") of the matrix. A positive value for the compaction rate can be thought of as a de-compaction, which describes a dilation of grains to allow melt into the pores. Likewise, a negative compaction rate corresponds to the situation where these grains are squeezing together to expel melt from the pores. Intuitively, the compaction rate will be some function of the pressure difference between the two phases. Further, when there is zero porosity, there can be no pressure difference, which would mean that the solid phase becomes incompressible. In this case we can write

$$P_f - P_m = \xi\nabla\cdot\mathbf{v}_m, \tag{15}$$

where the bulk viscosity modulates the compaction/dilation. (15) is compatible with what we obtained for the form of the stress tensor assumed in (13). At this point it is important to stress that the equations governing the motion of the two phases apply only to the average motion of the aggregate, on a scale considered to be larger than that of individual grains. The motion of individual grains cannot be described in this way.

We recall that our motivation was to express the force balance equation (7) in terms of the matrix velocity, which we can now do. Combining equations (9), (11) and (14) and substituting into (7) gives,

$$-\rho_m g(1-\phi)\delta_{i3} + \frac{\mu\phi^2}{K}(v_i^f - v_i^m) - P_f\frac{\partial\phi}{\partial x_i} + \frac{\partial}{\partial x_i}\left\{\left[-P_f\delta_{ij} + \xi\delta_{ij}\frac{\partial v_k^m}{\partial x_k} + \eta\left(\frac{\partial v_i^m}{\partial x_j} + \frac{\partial v_j^m}{\partial x_i} - \frac{2}{3}\delta_{ij}\frac{\partial v_k^m}{\partial x_k}\right)\right]\right\} = 0.$$

We can simplify this by substituting in (12). Expanding, combining pressure terms and absorbing a factor of into ξ and η then gives

$$\nabla P_f = \nabla\cdot\eta\left(\nabla\mathbf{v}_m + \nabla\mathbf{v}_m^T\right) + \nabla\left[\left(\xi - \frac{2}{3}\eta\right)\nabla\cdot\mathbf{v}_m\right] - \overline{\rho}g\hat{\mathbf{k}}, \tag{16}$$

where $\overline{\rho} = \rho_f\phi + \rho_m(1-\phi)$ is the phase-averaged density. We note that this is similar to the equation for incompressible Stokes' flow, except that now we are dealing with a compressible/compactible flow, which gives rise to an additional term accounting for compaction stresses.

To summarise, the governing equations are:

$$\frac{\partial(\rho_f\phi)}{\partial t} + \nabla\cdot\rho_f\phi\mathbf{v}_f = \Gamma \tag{17}$$

$$\frac{\partial\rho_m(1-\phi)}{\partial t} + \nabla\cdot\rho_m(1-\phi)\mathbf{v}_m = -\Gamma \tag{18}$$

$$\phi(\mathbf{v}_f - \mathbf{v}_m) = -\frac{K}{\mu}\nabla(P_f + \rho_f g z) \tag{19}$$

$$\nabla P_f = \nabla\cdot\eta\left(\nabla\mathbf{v}_m + \nabla\mathbf{v}_m^T\right) + \nabla\left[\left(\xi - \frac{2}{3}\eta\right)\nabla\cdot\mathbf{v}_m\right] - \overline{\rho}g\hat{\mathbf{k}} \tag{20}$$

2.3 Constituitive Equations

The unknown quantities that we are solving for are ϕ, P_f, P_m $\mathbf{v}_m$, and $\mathbf{v}_f$. We note that given $\mathbf{v}_m$, equation (12) decouples to give $\mathbf{v}_f$. Further, given P_f and $\mathbf{v}_m$, equation (15) decouples to give P_m, so we are essentially solve the system for P_f, $\mathbf{v}_m$ and ϕ.

The first simplification that we make is the Boussinesq approximation. This states that phase densities may be taken to be constant, except when multiplied by terms containing g. This is extended further to say that the phase densities are both equal to a mean density ρ, and that the density difference $\Delta\rho$ is neglected, except in buoyancy terms - here it is taken as a constant. Another common assumption that we make is to take the liquid viscosity μ to be

constant throughout. Realistically, however, this viscosity may depend on temperature and composition. Further, for simplicity we take the melting rate $\Gamma = 0$.

Now that we have our governing equations, we wish to close the system by imposing some constituitive relations for ρ_m, ρ_f, μ, K, Γ, ξ and η. We recall that permeability is assumed to be a function of porosity. In the limit of small porosity ($\phi << 1$) the permeability can be written as

$$K(\phi) = \frac{d^2}{c}\phi^n, \tag{21}$$

Here d is the grain size, and (c, n) are dimensionless constants that depend on the microstructure of the grains and pores. Looking at equation (12), we see that in order to ensure that relative velocity of the two phases increases with porosity, we require $n > 1$. In our present study we will take $n = 2$

It has been shown through experiment that the matrix shear viscosity η is a weakening function of porosity in addition to typical temperature and strain-rate behaviour. There remains some uncertainty about the martix bulk viscosity ξ; it is often assumed to be of similar magnitude to η, however for constant ρ_m, the bulk viscosity must tend to infinity as $\phi \to 0$. This is because the overall system must reduce to incompressible Stokes flow - for the solid phase - in this limit.

In the following, we shall relate the bulk viscosity $\xi(\phi)$ to the shear viscosity η simply as

$$\xi(\phi) = \tau_\xi \eta_0, \tag{22}$$

where $\tau_\xi = \frac{5}{3}$ (Takei Holtzman 2009 [21]) and $\eta_0 = \eta(\phi_0)$.

2.4 Nondimensionalisation

The next step is to non-dimensionalise the system. To do this we introduce scaled variables as follows,

$$\mathbf{X} = \frac{\mathbf{x}}{H}, \quad \mathbf{V} = \frac{\mathbf{v}_m}{U}, \quad P = (P_f + \rho g z)\frac{H}{\eta_0 U}, \quad K^* = \frac{K}{K_0} = (\frac{\phi}{\phi_0})^n, \quad \tau = t\frac{U}{H} \tag{23a}$$

$$\eta^* = \frac{\eta}{\eta_0}, \quad \xi^* = \frac{\xi}{\eta_0} \tag{23b}$$

In the above, H represents the characteristic length scale and U reprsents the characteristic velocity of the matrix, will vary depending on the specifics of the physical problem. We are considering the case of simple shear, with strain rate $\dot{\gamma}$, so that $U = \dot{\gamma} H$. The characteristic viscosity $\bar{\eta}$ is taken to be $\bar{\eta} = \xi_0 + 4\eta_0/3$, and the reference permeability K_0 is defined by $K_0 = K(\phi = \phi_0)$ with a reference melt fraction ϕ_0. The characteristic scale for the viscosity is motivated by the fact that, for constant viscosities η and ξ, equation (16) reduces to

$$\nabla P_f = -\eta \nabla \times \nabla \times \mathbf{v}_m + \left(\xi + \frac{4}{3}\eta\right)\nabla(\nabla \cdot \mathbf{v}_m) - \overline{\rho} g \hat{\mathbf{k}}, \tag{24}$$

In addition to this, we also define a reference compaction length δ_c and a nondimensional compaction length R by

$$\delta_c = \sqrt{\frac{(\xi_0 + 4\eta_0/3)K_0}{\mu}} = \sqrt{\frac{(\tau_\xi + \frac{4}{3})\eta_0 K_0}{\mu}}, \qquad R = \frac{\delta_c}{H}. \tag{25}$$

The compaction length is a natural length scale in magma/mantle dynamics; it depends on material properties of the melt and matrix, and represents a length scale over which perturbations to pressure differences decay to zero. We now introduce these scalings into our governing equations, and in doing so will be left with equations that contain only dimensionless parameters and variables. First we apply the Boussinesq approximation to (5), and - recalling that we have set $\Gamma = 0$ - obtain that

$$\frac{\partial \phi}{\partial t} = \nabla \cdot \left[(1-\phi)\mathbf{v}_m\right]. \tag{26}$$

In terms of the dimensionless variables this becomes

$$\frac{\partial \phi}{\partial \tau} = \nabla \cdot \left[(1-\phi)\mathbf{V}\right]. \tag{27}$$

Combining (26) and a similar expression for (4) (again, applying the Boussinesq approxmation), we have that

$$-\nabla \cdot \phi \mathbf{v}_f = \nabla \cdot \left[(1-\phi)\mathbf{v}_m\right]. \tag{28}$$

In which case,

$$\nabla \cdot \left[\phi \mathbf{v}_m - \phi \mathbf{v}_f\right] = \nabla \cdot \mathbf{v}_m. \tag{29}$$

Taking the divergence of (12) and substituting in (29), we obtain that

$$-\nabla \cdot \mathbf{v}_m = -\nabla \cdot \left[\frac{K}{\mu}\nabla(P_f + \rho_f g z)\right]. \tag{30}$$

Finally, introducing the scaled variables into the above gives

$$\nabla \cdot \mathbf{V} = \frac{R^2}{\tau_\xi + \frac{4}{3}} \nabla \cdot \left[(\frac{\phi}{\phi_0})^n \nabla P\right]. \tag{31}$$

Substituting the dimensionless variables into (16) we have that

$$\frac{U\eta_0}{H^2}\nabla P = \frac{U\eta_0}{H^2}\nabla \cdot \eta^* \left(\nabla \mathbf{V} + \nabla \mathbf{V}^T\right) + \frac{U\eta_0}{H^2}\nabla \left[\left(\xi^* - \frac{2}{3}\eta^*\right)\nabla \cdot \mathbf{V}\right]. \tag{32}$$

Cancelling and dropping stars we obtain the dimensionless version of (16)

$$\nabla P = \nabla \cdot \eta \left(\nabla \mathbf{V} + \nabla \mathbf{V}^T\right) + \nabla \left[\left(\xi - \frac{2}{3}\eta\right)\nabla \cdot \mathbf{V}\right]. \tag{33}$$

To summarize, the dimensionless system of governing equations is given by:

$$\boxed{\frac{\partial \phi}{\partial \tau} = \nabla \cdot \left[(1-\phi)\mathbf{V}\right]} \tag{34}$$

$$\boxed{\nabla \cdot \mathbf{V} = \frac{R^2}{\tau_\xi + \frac{4}{3}} \nabla \cdot \left[(\frac{\phi}{\phi_0})^n \nabla P\right]} \tag{35}$$

$$\boxed{\nabla P = \nabla \cdot \eta \left(\nabla \mathbf{V} + \nabla \mathbf{V}^T\right) + \nabla \left[\left(\xi - \frac{2}{3}\eta\right)\nabla \cdot \mathbf{V}\right]} \tag{36}$$

3 Discretisation

We begin by constructing the weak variational formulations for equations (34), (35) and (36). Considering equations (35) and (36) in conjuction with one another, we have something resembling Stokes' equations - these will be treated in the first section. In the subsequent section, we will consider the weak formulation and time-stepping of the advection equation (34). In the context of simple shear, we take the mesh to be a standard triangulation on a uniform rectangular grid. Periodic boundary conditions are imposed on the sides of the domain.

3.1 Discretisation of Stokes' equations

First, we shall provide definitions for the spaces that will be used. Throughout this section, we will refer to the Sobolev space $H^1(\Omega)$, which is defined by

$$H^1(\Omega) := \left\{V \in L^2(\Omega) : D^1 V \in L^2(\Omega)\right\} \tag{37}$$

Here D^1 denotes a weak derivative of order 1, and $L^2(\Omega)$ denotes the Lebesgue space of square-integrable functions on Ω. We now define the appropriate solution and test spaces for our finite element approximation,

$$H^1_E(\Omega) := \left\{V \in H^1(\Omega) : V = W \text{ on } \Gamma_D\right\}, \tag{38}$$

$$H^1_{E0}(\Omega) := \left\{V \in H^1(\Omega) : V = 0 \text{ on } \Gamma_D\right\}, \tag{39}$$

where W is a Dirichlet boundary condition, and Γ_D is the section of the boundary where the Dirichlet boundary condition is applied.

We multiply equation (35) through by a test function $Q \in L^2(\Omega)$ and integrate over the domain. This gives

$$\int_\Omega Q \nabla \cdot \mathbf{V} \mathrm{d}x = \int_\Omega Q \frac{R^2}{\tau_\xi + \frac{4}{3}} \nabla \cdot \left[(\frac{\phi}{\phi_0})^n \nabla P \right] \mathrm{d}x. \tag{40}$$

The natural boundary condition comes from the impermeability at the boundaries, and so the gradient of the pressure normal to the boundary is taken to be zero. Therefore, integrating by parts the RHS gives

$$\int_\Omega Q \nabla \cdot \mathbf{V} \mathrm{d}x = -\int_\Omega \frac{R^2}{\tau_\xi + \frac{4}{3}} \nabla Q \cdot \left[(\frac{\phi}{\phi_0})^n \nabla P \right] \mathrm{d}x. \tag{41}$$

(36) can be modified to be

$$\nabla \cdot \eta \left(\nabla \mathbf{V} + \nabla \mathbf{V}^T \right) + \nabla \left[\left(\xi - \frac{2}{3}\eta \right) \nabla \cdot \mathbf{V} \right] - \nabla P = \mathbf{f}, \tag{42}$$

where f is understood to be identically zero (for each component) on the Ω. Multiplying equation (42) through by a test function $\mathbf{U} \in H^1_{E0}(\Omega)$ and integrating over the domain gives

$$-\int_\Omega \mathbf{U} \cdot \left[\nabla \cdot \eta \left(\nabla \mathbf{V} + \nabla \mathbf{V}^T \right) \right] \mathrm{d}x + -\int_\Omega \mathbf{U} \cdot \nabla \left[\left(\xi - \frac{2}{3}\eta \right) \nabla \cdot \mathbf{V} \right] \mathrm{d}x + \int_\Omega \mathbf{U} \cdot \nabla P \mathrm{d}x = \int_\Omega \mathbf{U} \cdot \mathbf{f} \mathrm{d}x.$$

(43)

Integrating by parts for each term on the LHS gives

$$\int_\Omega \eta \nabla \mathbf{U} : \left(\nabla \mathbf{V} + \nabla \mathbf{V}^T\right) \mathrm{d}x + \int_\Omega (\xi - \frac{2}{3}\eta)(\nabla \cdot \mathbf{U})(\nabla \cdot \mathbf{V}) \mathrm{d}x - \int_\Omega (\nabla \cdot \mathbf{U}) P \mathrm{d}x = \int_\Omega \mathbf{U} \cdot \mathbf{f} \mathrm{d}x \quad (44)$$

Re-writing the first term on the LHS in a form which is symmetric is done by replacing $\nabla \mathbf{U}$ with

$$\frac{1}{2}\left(\nabla \mathbf{U} + \nabla \mathbf{U}^T\right). \quad (45)$$

This gives the same result when taking the inner product with $\nabla \mathbf{V} + \nabla \mathbf{V}^T$. The reason for this is that, if we take the inner product $\mathbf{A} : \mathbf{B}$, where $\mathbf{B}$ is symmetric, then the inner product only "sees" the symmetric part of $\mathbf{A}$. We neglect the proof of this fact. Adopting this new form and combining it with (44), we have the weak formulation for Stokes' equations: *Find a* $V \in H^1_E$ *and a* $P \in L^2(\Omega)$ *such that:*

$$\begin{aligned} &\int_\Omega \frac{\eta}{2}\left(\nabla \mathbf{U} + \nabla \mathbf{U}^T\right) : \left(\nabla \mathbf{V} + \nabla \mathbf{V}^T\right) \mathrm{d}x + \int_\Omega (\xi - \frac{2}{3}\eta)(\nabla \cdot \mathbf{U})(\nabla \cdot \mathbf{V}) \mathrm{d}x \\ &- \int_\Omega (\nabla \cdot \mathbf{U}) P \mathrm{d}x - \int_\Omega \frac{R^2}{\tau_\xi + \frac{4}{3}} \nabla Q \cdot \left[(\frac{\phi}{\phi_0})^n \nabla P\right] \mathrm{d}x - \int_\Omega Q \nabla \cdot \mathbf{V} \mathrm{d}x = \int_\Omega \mathbf{U} \cdot \mathbf{f} \mathrm{d}x, \\ &\qquad\qquad \forall U \in H^1_{E0} \text{ and } \forall Q \in L^2(\Omega). \end{aligned} \quad (46)$$

To write this in a more convenient form, we define the operator $a : H^1(\Omega) \times H^1(\Omega) \to \mathbb{R}$, the continuous bilinear forms $b : H^1(\Omega) \times L^2(\Omega) \to \mathbb{R}$ and $c : L^2(\Omega) \times L^2(\Omega) \to \mathbb{R}$, and the linear functional $l : H^1(\Omega) \to \mathbb{R}$ as:

$$a(V, U; \phi) := \int_\Omega \frac{\eta}{2}\left(\nabla \mathbf{U} + \nabla \mathbf{U}^T\right) : \left(\nabla \mathbf{V} + \nabla \mathbf{V}^T\right) \mathrm{d}x + \int_\Omega (\xi - \frac{2}{3}\eta)(\nabla \cdot \mathbf{U})(\nabla \cdot \mathbf{V}) \mathrm{d}x, \quad (47)$$

$$b(U, Q) := -\int_\Omega Q \nabla \cdot \mathbf{V} \mathrm{d}x, \quad (48)$$

$$c(P, Q; \phi) := -\int_\Omega \frac{R^2}{\tau_\xi + \frac{4}{3}} \nabla Q \cdot \left[(\frac{\phi}{\phi_0})^n \nabla P\right] \mathrm{d}x, \quad (49)$$

$$l(U) := \int_\Omega \mathbf{U} \cdot \mathbf{f} \mathrm{d}x \quad (50)$$

This allows us to express (46) in a more condensed form as: *Find a* $V \in H^1_E$ *and a* $P \in L^2(\Omega)$ *such that:*

$$\begin{aligned} &a(V, U; \phi) + b(V, Q) + b(U, P) + c(P, Q; \phi) = l(U), \\ &\qquad\qquad \forall U \in H^1_{E0} \text{ and } \forall Q \in L^2(\Omega). \end{aligned} \quad (51)$$

We select finite dimensional spaces, $X^h_0 \subset H^1_{E0}(\Omega)$ and $M_h \subset L^2(\Omega)$, in which to cast the discretised problem. Taking the discretised solution space for the velocity to be X^h_E we have the following mixed variational approximation: *Find a* $V \in H^1_E$ *and a* $P \in L^2(\Omega)$ *such that:*

$$\begin{aligned} &a(V_h, U_h; \phi_h) + b(V_h, Q_h) + b(U_h, P_h) + c(P_h, Q_h; \phi_h) = l(U_h), \\ &\qquad\qquad \forall U_h \in X^h_0 \text{ and } \forall Q_h \in M_h(\Omega). \end{aligned} \quad (52)$$

3.2 Discretisation of the advection equation

We now construct the discretisation for the advection equation (34). Once again, multiplying through by a test function W and integrating over Ω gives

$$\int_\Omega W \frac{\partial \phi}{\partial \tau} \mathrm{d}x = \int_\Omega W \nabla \cdot [(1-\phi)\mathbf{V}] \, \mathrm{d}x \tag{53}$$

The weak formulation for the advection equation can then be stated as: *Find a* $\phi \in H^1(\Omega)$ *such that:*

$$\int_\Omega W \frac{\partial \phi}{\partial \tau} \mathrm{d}x = \int_\Omega W \nabla \cdot [(1-\phi)\mathbf{V}] \, \mathrm{d}x, \ \forall W \in L^2(\Omega) \tag{54}$$

As before, we aim to restate this more concisely by introducing an operator $d: \ H^1(\Omega) \ \rightarrow \mathbb{R}$. We define d to be

$$d(\phi, W; V) := -\int_\Omega W \nabla \cdot [(1-\phi)\mathbf{V}] \, \mathrm{d}x \tag{55}$$

Casting the discrete weak formulation in terms of the finite dimensional space $S^h \subset H^1(\Omega)$, where S^h is a given solution space for the porosity, allows the discretised problem to be stated as: *Find a* $\phi_h \in S^h$ *such that:*

$$\int_\Omega W_h \frac{\partial \phi_h}{\partial \tau} \mathrm{d}x + d(\phi_h, W_h; V_h) = 0, \ \forall W_h \in S^h \tag{56}$$

We approximate the time derivative by a Crank-Nicolson scheme, so that the problem is to find $\phi_h^k \in S^h$ for $0 \leq k \leq N$, such that:

$$\int_\Omega W_h \frac{\phi_h^{k+1} - \phi_h^k}{\Delta t} \mathrm{d}x + \frac{1}{2}\left[d(\phi_h^k, W_h; V_h^k) + d(\phi_h^{k+1}, W_h; V_h^k) \right] = 0, \ \forall W_h \in S^h, \tag{57}$$

where $\Delta t = 1/N$.

4 Code Benchmarking

The next task is to build a robust code that can produce a reliable numerical simulation of the model. To benchmark the code, we choose the well documented problem of modeling a two-phase compactable flow under simple shear [19], [7]. For the set-up (see Figure 1) we used a rectangular domain, with a dimensonless spatial ratio of 2×1. The boundary conditions are

$$\mathbf{V} = (1/2)\mathbf{i}, \ Y = 1 \qquad \mathbf{V} = -(1/2)\mathbf{i}, \ Y = 0 \qquad k_\phi = 0, \ Y = 0, \ 1 \tag{58}$$

Further, periodic boundary conditions are imposed for $\mathbf{V}$, P and ϕ on the left and right boundaries, to resemble an infinite domain in the x-direction. The problem is discretised in space with Taylor-Hood P2/P1 elements. Using this discretisation with the weak formulation

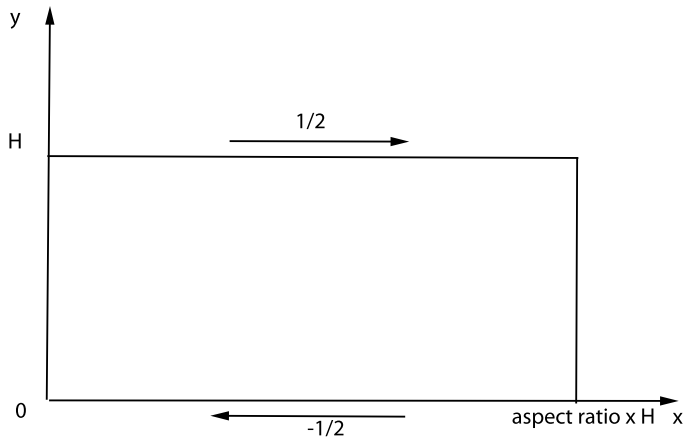

Figure 1: *Schematic of the domain for simple shear flow. The top boundary at $x = H$ is an impermeable boundary with no-slip boundary conditions, and the left/right boundaries are periodic. The dimensionless shear-strain rates at the top and bottom are $\frac{1}{2}$ and $-\frac{1}{2}$ respectively.*

derived above, FEniCS [9] is used to solve the PDEs (34)-(36). We use a built-in non-linear solver, which automatically applies a Newton method to the non-linear PDE.

To benchmark the code, results from the numerical simulations are compared to the results from the linear analysis presented in Spiegelman 2003 [19]. The equations (34)-(36) are linearised about a uniform porosity field, with a small harmonic perturbation applied to this background state by taking $\phi = \phi_0 + \epsilon\phi_1$, where

$$\phi_1 = e^{i\mathbf{k}(t)\cdot\mathbf{x}+s(t)}. \tag{59}$$

$s(t)$ is the growth rate of this perturbation, and $\mathbf{k}(t)$ is a time-dependent wave vector given by

$$\mathbf{k}(t) = k_x^0\mathbf{i} + (k_y^0 - k_y^0 t)\mathbf{j}, \tag{60}$$

where k_x^0 and k_y^0 come from the definition of the intial wave vector $\mathbf{k_0} = (k_x^0, k_y^0)$. The initial wave-number k_0 is defined by $k_0 = |\mathbf{k}_0|$, and the angle of the plane wave to the plane of shear is given by $\theta(t) = \tan^{-1}(\frac{k_x^0}{k_y(t)})$. By substituting the linearised variables into the full non-linear equations, an analytical equation for the instantaneous growth rate of the perturbation can be obtained as

$$\frac{ds}{dt} = \frac{2\lambda\eta_0}{\tau_\xi + 4/3}(1-\phi_0)\frac{k_x k_y}{k^2+1}. \tag{61}$$

We use this expression as a basis for benchmarking the code. To make a direct comparison between (61) and the numerical solution, we must preserve the relevant scalings in the

Table 1: Constant Viscosity Test Case

Parameter	Symbol	Value
Bulk/shear viscosity ratio	τ_ξ	5/3
Reference compaction length	R	1
Porosity weakening factor	λ	0
Permeability exponent	n	2
Initial uniform porosity	ϕ_0	0.05
Initial amplitude of porosity perturbation	Ψ	0.0001
Initial perturbation angle	θ_0	$\pi/6$
Viscosity coefficient	η_0	1
Initial wave number	k_0	4π

derivation of the full nondimensional equations. It turns out that the nondimensionalisation in section 2.4 can be made identical by taking the reference compaction length $R = 1$. This is equivalent to taking $H = \delta_c$.

Taking a first-order balance of terms we have that $\dot{s}$ is related to the first-order compaction rate $\mathcal{C}_1$ by

$$\dot{s} = \left.\frac{d \ln \phi_1}{d\tau}\right|_{\tau=0} = -\mathcal{C}_0 + (1-\phi_0)\frac{\mathcal{C}_1}{\phi_1}. \tag{62}$$

For simple shear, it is the case that $\mathcal{C}_0 = 0$. In this case we have an instantaneous numerical growth rate is given by

$$\dot{s} = (1-\phi_0)\frac{\nabla \cdot \mathbf{V}}{\phi_1}. \tag{63}$$

In our code the initial porosity perturbation is taken to be of the form

$$\phi = \phi_0 + \Psi \cos(k_0(x \sin(\theta_0) + y \cos(\theta_0))), \tag{64}$$

where the values of Ψ, ϕ_0, k_0 and θ_0 are given in Table 1. Using this form for the perturbation, and calculating (63) at a point at the centre of the domain [8] gives

$$\dot{s} = (1-\phi_0)\frac{\nabla \cdot \mathbf{V}}{\Psi}. \tag{65}$$

4.1 Results

We initially take $\lambda = 0$, so that the shear viscosity η is constant. In this case there is no feedback between the porosity and viscosity, so that the harmonic perturbation is only sheared by the background flow. The parameter values that are used for the simulation are given in are given above (Table 1). The time-step is taken to be $\Delta t = 5 \times 10^{-2}$, run until a final time of $T = 3$. Furthermore, the height of the grid is taken to be $H = 1$, and the width $AH = 4$. The resolution of the grid is taken to be $100(i) * 50(j)$ grid cells. In Figure 2 we see a gradual rotation of the bands, caused by the shearing at the boundaries.

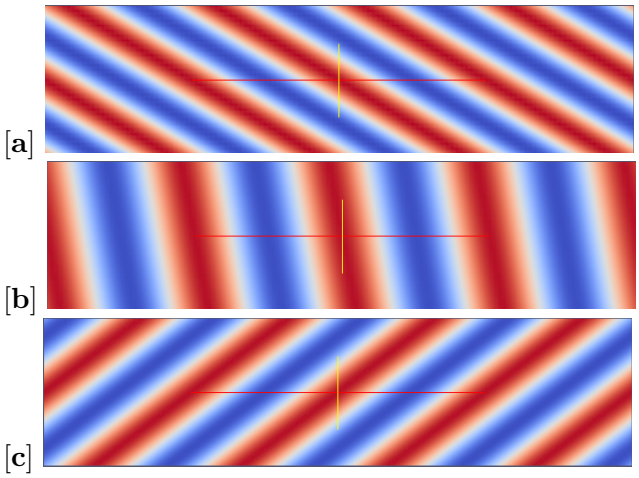

Figure 2: *Snapshots of porosity evolution for a constant shear viscosity, with a small initial harmonic perturbation. (**a**) T=0, (**b**) T=1.5, (**c**) T=3*

We now turn our attention to the case of a porosity weakening shear viscosity, given by $\eta(\phi) = \eta_0 e^{\lambda(\phi-\phi_0)}$. The parameters used in the simulation are given Table 1, except that the porosity weakening factor λ is taken to be $\lambda = -1$. In reality $\lambda \approx -27$, but to moderate the porosity weakening we take a small magnitude value for λ. The resulting simulation for the evolution of the porosity is given in Figure 3. These snapshots show that the growth of bands for angles in the interval $0°<\theta<90°$. As the bands are rotated in the region $\theta>90°$, the growth of the bands is reversed and they begin to constrict. This is in agreement with [19].

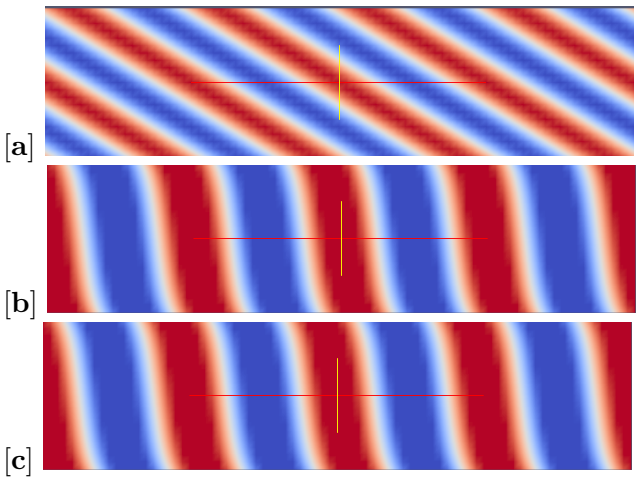

Figure 3: *Snapshots of porosity evolution (with harmonic perturbation) for a porosity weakening shear viscosity, with factor $\lambda = -1$. (**a**) T=0, (**b**) T=1.5, (**c**) T=3*

Using the results from this simulation, we validate the elliptic part of the code by comparsion with the instantaneous growth rate given in equation (61). We recall that the the instanteous growth rate of the perturbation is taken at the centre of the domain by $\dot{s} = (1-\phi_0)\frac{\nabla\cdot\mathbf{V}}{\Psi}$. The mesh resolution is taken to be $200(i) * 100(j)$ grid cells, and an initial wave-number of $k_0 = 24\pi$. Using this, the numerical instantaneous growth rate is calculated, based on the

computed velocity $\mathbf{V}$ at the centre of the domain. This is repeated over a sequence of different initial band orientation angles θ_0. Figure 4 shows these results for a range of angles between 0 and 180°. From this plot it is clear that the elliptic part of our model is valid. In particular, the code predicts maximum growth of bands oriented at 45° to the shear plane.

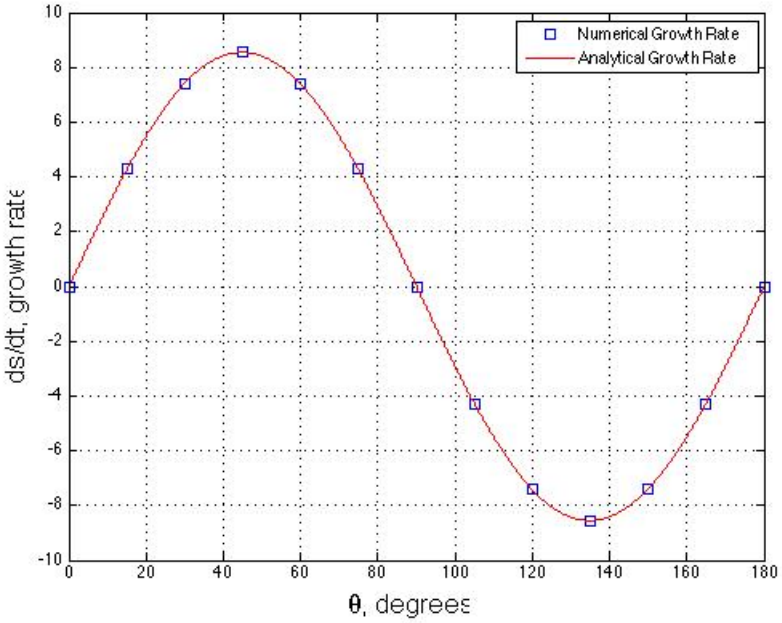

Figure 4: *Here we compare the numerical and analytical perturbation growth rates at t=0, varying the initial perturbation angle from* 0 *to* 180°. *We calculate the instantaneous numerical growth rate at intervals of* 15°. *The red-line corresponds to growth rate from the linear analysis. The resolution of the grid is* $200(i) * 100(j)$ *cells.*

4.2 Anisotropic Viscosity

Theoretical work by Stevenson (1989) [20] predicts the spontaneous assembly of a banded structure, as is seen in simple shear experiments. There are, however, key experimental observations that are not satisfied by the model in [11]. More recently, approaches (Katz et al. (2006) [7]) have been adopted to extend the standard model and reconcile these observations. A new alternative approach, presented in Katz/Takei [23], extends assumptions of the model to include anisotropy of matrix viscosity at the continuum level. This theory is based on work by Takei and Holtzman ([21], [22]), in which constituitive laws for anisotropic viscosity of the two-phase system are derived. A key feature of this new theory is that it predicts the emergence of porosity bands - oriented at $15 - 20°$ to the shear plane - independent of stress, strain rate or whether the flow is by diffusion or dislocation creep. This is in agreement with the experimental observations (Zimmerman et al. (1999) [24], Holtzman et al. (2003b) [5] and Holtzman/Kohlstedt (2007) [6].) The code is altered to incorporate viscous anisotropy, based on the formulation in [23].

In terms of the model equations, this modifies (36) to become

$$P_{,i} = (C_{ijkl}\dot{\epsilon}_{kl})_{,j}. \tag{66}$$

C_{ijkl} is the viscosity tensor, defined as

$$C_{ijkl} = e^{-\lambda(\phi-\phi_0)}\left[\left(\tau_\xi - \frac{2}{3}\right)\delta_{ij}\delta_{kl} + \delta_{ik}\delta_{jl} + \delta_{il}\delta_{jk} - \alpha a_{ix_g}a_{jx_g}a_{kx_g}a_{lx_g}\right], \tag{67}$$

where α is the magnitude of anisotropy and a is the rotation matrix defined by:

$$\begin{bmatrix} cos\Theta & -sin\Theta \\ sin\Theta & cos\Theta \end{bmatrix} \tag{68}$$

Here $(x_g,\ y_g)$ refer to grain coordinates that are defined independently of the continuum coordinates (x, y), and Θ is the angle from the x_g axis to the x axis. The j-th grain coordinate refers to the j-th column of the matrix a.

To derive the weak formulation is very similar to the case of no anisotropy. We can consider just the anisotropic part of the stress tensor and derive its weak formulation - the rest follows from section 3.

The ij-th component of the anisotropic part of the stress tensor is given by (adopting the summation convention)

$$-(\alpha\eta a_{ix_g}a_{jx_g}a_{kx_g}a_{lx_g}\dot{\epsilon}_{kl}) \tag{69}$$

where $\dot{\epsilon}_{kl}$ is the strain rate tensor. If we were to include the anisotropic part of the stress tensor in equation (10), it would be of the form

$$-(\alpha\eta a_{i1}a_{j1}a_{k1}a_{l1}\dot{\epsilon}_{kl})_{,j} \tag{70}$$

Multiplying through by a test function $\mathbf{U} \in H^1_{E0}(\Omega)$ and integrating over the domain gives

$$-\int_\Omega U_i(\alpha\eta a_{i1}a_{j1}a_{k1}a_{l1}\dot{\epsilon}_{kl})_{,j}\,\mathrm{d}x_i. \tag{71}$$

We define a second rank tensor $\mathbf{\Sigma}$ such that $(\mathbf{\Sigma})_{ij} = \alpha\eta a_{i1}a_{j1}a_{k1}a_{l1}\dot{\epsilon}_{kl}$. Integrating the above by parts and applying Gauss' theorem gives

$$\int_\Omega \epsilon(\mathbf{U}) : \mathbf{\Sigma}\mathrm{d}x, \tag{72}$$

where $\epsilon(\mathbf{U})$ is the symmetric gradient of $\mathbf{U}$. Combining the above with what is derived in section 3, we have the weak variational formulation for the "Stokes" equations: *Find a* $V \in H^1_E(\Omega)$ *and a* $P \in L^2(\Omega)$ *such that:*

$$\begin{aligned} &-\int_\Omega (\nabla\cdot\mathbf{U})P\mathrm{d}x + \int_\Omega \epsilon(\mathbf{U}) : \eta\left(\nabla\mathbf{V} + \nabla\mathbf{V}^T\right)\mathrm{d}x \\ &+\int_\Omega \left(\tau_\xi - \frac{2}{3}\right)\eta(\nabla\cdot\mathbf{V})(\nabla\cdot\mathbf{U})\mathrm{d}x \\ &-\int_\Omega \epsilon(\mathbf{U}) : \mathbf{\Sigma}\mathrm{d}x - \int_\Omega Q\nabla\cdot\mathbf{V}\mathrm{d}x - \int_\Omega \frac{R^2}{\tau_\xi + \frac{4}{3}}\nabla Q\cdot\left[(\frac{\phi}{\phi_0})^n(\nabla P)\right]\mathrm{d}x = 0, \\ &\qquad\qquad \forall\mathbf{U} \in H^1_{E0} \text{ and } \forall Q \in L^2(\Omega). \end{aligned} \tag{73}$$

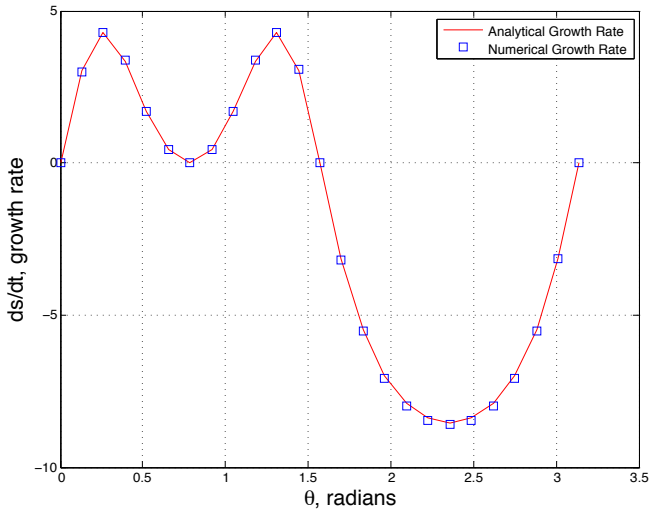

Figure 5: *Comparison between the numerical and analytical instantaneous growth rates of a small harmonic perturbation. Anisotropy parameters are* $\alpha = 2$, $\Theta = \pi/4$.

The discretisation of the advection equation is identical to the isotropic case, so we neglect its derivation here.

To validate the elliptic equations in our code we compute the growth rate of a small harmonic perturbation to an initially uniform background porosity field. This growth rate is calculated instantaneously at $t = 0$, and is then compared with the growth rate obtained from the stability analysis in [8]. These calculations are for $KR = 75$, $\alpha = 2$, $\Theta = \pi/4$, $\lambda = -27$ and $\tau_\xi = 5/3$. The resolution of the domain is 200(i)*100(j) grid cells. The results are plotted in Figure 5. The numerical simulations match up well with the results from the linear stability analysis, which gives reasonable grounds to suggest that the elliptic part of the code is functioning well.

4.3 Diffusion in the model

A problem with the model in [11] is that for simulations that run for large strains, the porosity takes values that are physically irrelevant. Currently, there is no consensus on how to resolve this, however some success has been achieved by including a diffusion term in the advection equation (34). The general form of the diffusion term is $\nabla \cdot \epsilon \nabla \phi$. A general form for ϵ that we experimented with was of the form $\epsilon = \epsilon_0 |\nabla \phi|^m |\dot{\gamma}|^p$, where ϵ_0, m and p are unknown parameters. In simulations, the addition of the strain rate dependency in the term $|\dot{\gamma}|^p$ creates difficulties in running for large strains, so we neglect this and take $p = 0$. This term then becomes $\epsilon = \epsilon_0 |\nabla \phi|^m$. The values of ϵ_0 and m are not known, but throughout this document we take $\epsilon_0 = 0.1$ and $m = 2 - 4$. These values for m give reasonable amount of diffusion, with a higher diffusion for a larger m. Taking this form for the diffusion term means that the

advection equation equation (34) becomes

$$\frac{\partial \phi}{\partial \tau} = \nabla \cdot [(1-\phi)\mathbf{V}] + \nabla \cdot (\epsilon_0 |\nabla \phi|^m \nabla \phi). \tag{74}$$

This addition of this term in the weak formulation is trivial. Throughout this document, we refer explicitly to cases where diffusion is included.

4.4 Anisotropic viscosity - Forward model

We integrate viscous anisotropy and the diffusion term into numerical model, and use FEniCS to solve the discretised problem. The parameters of the simulation are taken to be $\tau_\xi = 5/3$, $\lambda = -27$, $R = 0.1$, $\phi_0 = 0.05$ and $m = 3.3$. The mesh resolution is taken to be $200(i) * 100(j)$ grid cells, with a time-step of $\Delta t = 10^{-2}$. The advantage of the diffusion term is that it permits the simulation to run for larger strains. Figure 6 show the evolution of the porosity for a strain of $\gamma = 2$. The initial condition was taken to be a random noise perturbation, where the value of ϕ takes the value of the random variable $\mathbf{X} = 0.05 + \mathbf{Y}$. Here $\mathbf{Y}$ is a random Gaussian distribution on the interval $(-0.01, 0.01)$. The set-up is simple shear with the same domain size and boundary conditions as for the isotropic case in (58). The assumption of fixed anisotropy is made with $\alpha = 2$ and $\Theta = \pi/4$. Referring to Figure 6, we see a gradual assembly of the system into high porosity bands, oriented at $15 - 20^\circ$ to shear plan, which coincides with experimental observations [5]. Figures 6**f**- 6**h** show reconnections between bands, which is a robust experimental observation [6]. This network of bands is thought to be a mechanism that helps maintain a "statistical" steady state of low angle $(15 - 20^\circ)$ bands. The growth of bands is reduced as they are sheared and rotated (past 20°) by the background flow, and the system tends to "return" to this low angle state. A network of bands forms so that the melt from the bands in less favourable positions (in terms of growth) can transport melt into lower angle bands, where growth is optimal.

In conclusion, we have successfully built a code that can reproduce results predicted by theory, including the addition of viscous anisotropy. Further, the formation of bands and the evidence of band reconnection is evident in the simulations, with an encouraging resemblance to experimental observations. Having demonstrated the codes capability to reproduce observations, we move to extend it with dolfin-adjoint. At this point, the motivation is to be able to use generalised stability theory to identify the porosity perturbations that grow optimally for finite strains. In the next section we introduce this theory.

5 Generalised Stability Theory

5.1 Theory

The traditional method for analysing the stability of a nonlinear mechanical system was pioneered by Lyapunov [10]. This general approach is to linearise the system about some base-state, and to compute the eigenvalues of the resulting system. Depending on whether the real parts of the eigenvalues are positive or negative, one can classify the system accordingly. However, this approach only ascertains the asymptotic stability of the system, as $t \to \infty$.

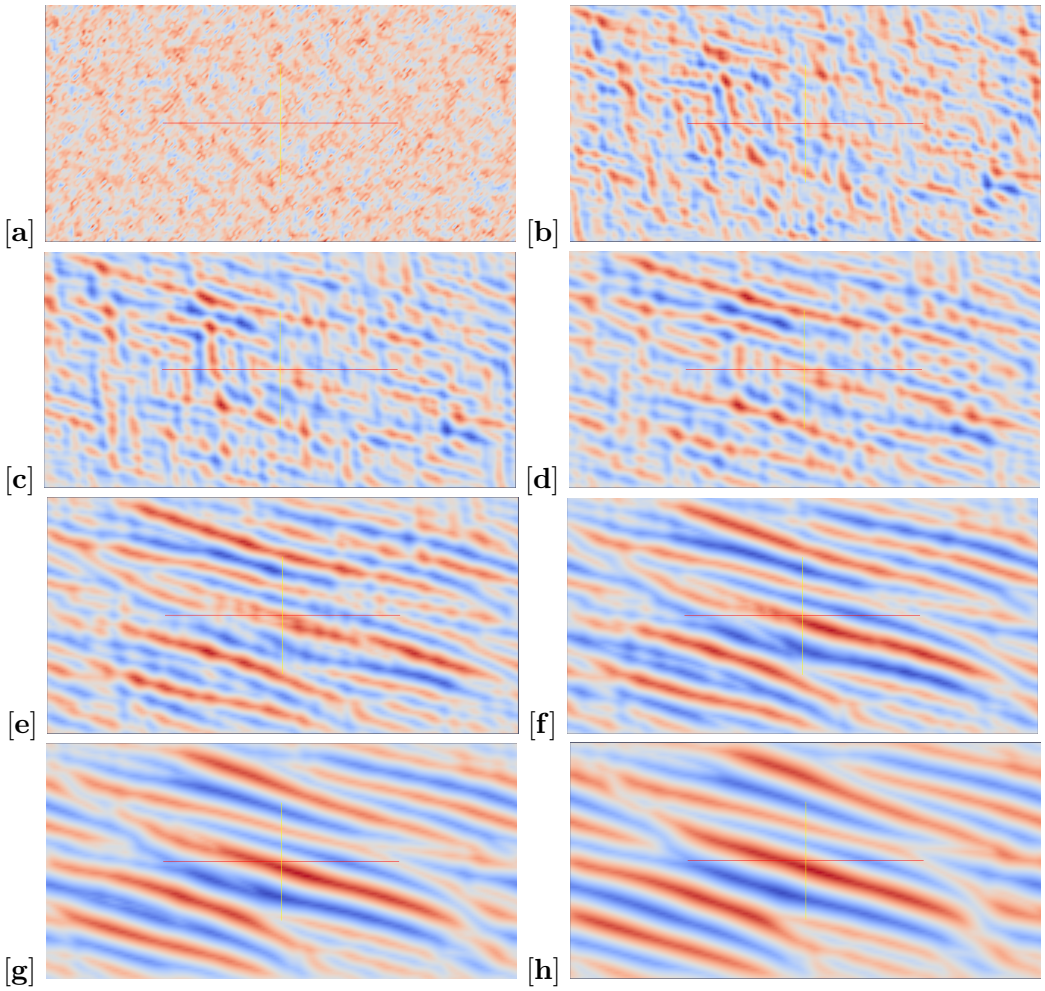

Figure 6: *Snapshots from simluation of porosity evolution with anisotropic viscosity. Parameters are* $\lambda = -27$, $R = 1$, $m = 3.3$ *and* τ_ξ. *Mesh resolution is* $200(i)*100(j)$ *grid cells with time-step* $\Delta t = 10^{-2}$. ***(a)*** *shows the initial condition, and* ***(b)****-****(h)*** *show the evolved porosity for every 25 time-steps.*

If the linearised system is non-normal; that is, its eigenfunctions do not form an orthogonal basis [16], then a "stable" system may permit a trasient deviation before decaying back to a steady state.

The occurence of non-normal systems in a range of disciplines was motivation for the development of a finite time theory of stability, presented in *B. Farrell et al.* [2], [3]. We follow the exposition in [14] by considering the propagator of the system. To introduce the notion of the "propagator" we consider the solution of a system at time T, u_T, as a function of some intial condition u_0. The operator that maps this initial condition to the final state is defined by

$$u_T = M(u_0), \tag{75}$$

where M is the *nonlinear propagator*. The idea is to now linearise this operator about the given solution trajectory, which is done by adding on some small perturbation δu_0 to the

initial condition u_0. The resulting change in the final state is given by

$$\delta u_T = M(u_0) + \frac{dM}{du_0}\delta u_0 + \mathcal{O}((\delta u_0)^2) - M(u_0). \tag{76}$$

Simplifying and neglecting terms of $\mathcal{O}(\delta^2)$ or greater, we obtain the linearised perturbation to the final state as

$$\delta u_T \approx \frac{dM}{du_0}\delta u_0. \tag{77}$$

We define the linearised propagator L by

$$L \equiv \frac{dM}{du_0}. \tag{78}$$

We want to find perturbations δu_0 that grow the most over the finite time period $[0, T]$.

The initial perturbation δu_0 that we seek satisfies

$$\delta u_0 = \arg\max \, \langle \delta u_T, \delta u_T \rangle \, , \, ||\delta u_0|| = 1 \tag{79}$$

where, for simplicity, the inner product is taken to be the standard inner product with norm $||\delta u_0|| = \sqrt{\langle \delta u_0, \, \delta u_0 \rangle}$. In terms of the propagator, (79) becomes

$$\langle \delta u_T, \, \delta u_T \rangle = \langle L\delta u_0, \, L\delta u_0 \rangle = \langle \delta u_0, \, L^* L \delta u_0 \rangle. \tag{80}$$

Clearly then, the optimally growing perturbation is the leading eigenfunction of L^*L; that is, the eigenfunction of L^*L associated with the largest eigenvalue μ. The norm of the perturbation is given by $\sqrt{\mu}$.

We briefly re-cap the concept of a matrix singular value decomposition. Given a matrix A, and its SVD:

$$A = U\Sigma V^*, \tag{81}$$

where U and V are unitary matrices and Σ is rectangular diagonal with non-negative real entries. Using the above we can write

$$A^*A = U(\Sigma\Sigma^*)V^*, \tag{82}$$

where $\Sigma\Sigma^*$ is a diagonal matrix with entries corresponding to the eigenvalues of A^*A, and V has the eigenvectors of A^*A as its columns. This motivates the use of the SVD to obtain the eigenfunctions and eigenvalues of the linearised propagator.

We can make the analysis in this section more general by consider the initial condition and final solution spaces are equipped with the inner products $\langle \cdot, \cdot \rangle_I \equiv \langle \cdot, X_I \cdot \rangle$ and $\langle \cdot, \cdot \rangle_F \equiv \langle \cdot, X_F \cdot \rangle$ respectively. In order to define an inner product the operators X_I and X_F must both be positive definite symmetric. In this general setting, the non-zero singular values of L are the square roots of the non-zero eigenvalues of $X_I^{-1}L^*X_FL$, and these corresponding eigenfunctions and eigenvalues can be found from the generalised SVD. We can interpet these singular values in the following way by considering some singular function v and corresponding singular value σ: if $\sigma > 1$ then the perturbation will grow over the finite time period, and if $\sigma < 1$ then this perturbation will decay.

5.2 Computing the propagator

The nonlinear propagator M is generally not available as an explicit function, but will be implicitly embedded in the solution of some PDE. We let m be some parameter, which for generality is assumed to be some initial condition. Letting the solution be denoted by u (we let $u_0 = m$), the implicit form of the PDE can be written as

$$F(u, m) = 0. \tag{83}$$

Differentiating the above with respect to m we obtain the relation:

$$\frac{\partial F(u,m)}{\partial u}\frac{du}{dm} + \frac{\partial F(u,m)}{\partial m} = 0 \tag{84}$$

This is the so called "tangent-linear" equation associated with $F(u, m) = 0$, and we solve for the Jacobian $\frac{du}{dm}$. This solution describes how the solution changes with the initial condition m. As we assume that the nonlinear propagator M can be computed to return the solution at any time T, we can think of it as

$$\left.\frac{du}{dm}\right|_T = \frac{dM}{dm} \tag{85}$$

Solving the tangent-linear equation would give us that

$$\left.\frac{du}{dm}\right|_T = -\left.\frac{\partial F(u,m)}{\partial u}^{-1}\frac{\partial F(u,m)}{\partial m}\right|_T. \tag{86}$$

We recall the definition of the linearised propagator L in equation (78). Suppose now that we have some perturbation to the initial condition δm, and we want to evaluate the action of L on δm. This is then equivalent to solving the tangent-linear equation, evaluating at time T, and then applying this solution operator to the perturbation δm. This is written as

$$L\delta m \equiv -\left.\frac{\partial F(u,m)}{\partial u}^{-1}\frac{\partial F(u,m)}{\partial m}\delta m\right|_T. \tag{87}$$

We can summarise the generalised stability analysis of the PDE $F(u, m) = 0$ as follows:

1) Derive and solve the tangent linear system associated with the PDE to obtain the propagator L.

2) Derive and solve the adjoint of the tangent linear system to obtain the adjoint propagator L^*.

3) Once L and L^* are available, compute the SVD of L.

5.3 Simple Shear

We use the framework of generalised stability theory to investigate perturbations to a uniform porosity field under simple shear. The code is extended to calculate the SVD through dolfin-adjoint and FEniCS. Dolfin-adjoint automatically derives the tangent-linear and adjoint

equations, and the calculation may involve many iterative solves of these equations. The outputs of the calculation are the eigenfunctions, growth rates, and the evolved eigenfunctions for the final solution time specified.

The principal field of interest is the porosity, and a natural "base-state" to choose a uniform state throughout the domain. Using the code for simple shear, we can then utilise dolfin-adjoint to automate the GST calculation. This calculation is designed to give the optimally growing perturbations to this uniform porosity field, for a specific final time T. These calculations were initially performed for the case of isotropic viscosity with $T = 10\Delta t$, where $\Delta t = 10^{-2}$. The parameters associated with this calculation were $R = 1$, $\lambda = -27$, $\tau_\xi = 5/3$, and $\phi_0 = 0.05$. The grid resolution was taken to be $60(i) * 30(j)$ grid cells. Figure 7 shows the results for the 0th eigenfunction in this calcultion. This corresponds to the optimally growing perturbation to the base-state over $[0,\ T]$, and here we can see that the optimal perturbation is given by bands at approximately $35 - 40^\circ$ to the shear plane. From [19] and the results of our numerical simulation, the optimal growth of bands is experienced at 45° to the shear plane. Therefore, for larger strains we'd expect the angle of the bands in the optimal perturbation to be less than 45°, as these will be gradually rotated into a favourable position, and experience optimal growth. This result complements the results of the random intial condition simulations which show the emergence of bands, by showing that bands are the dominant instability.

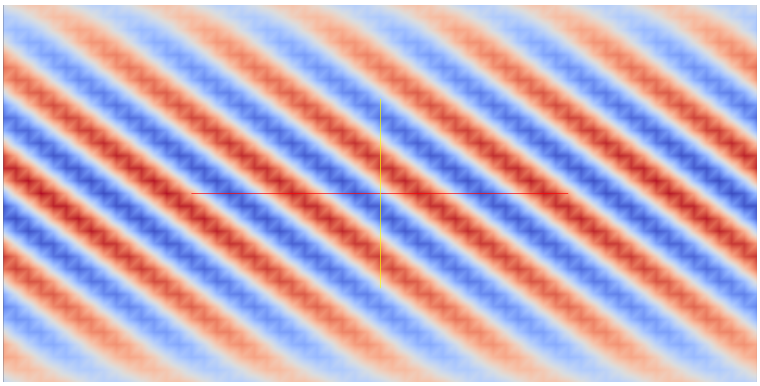

Figure 7: *0th eigenfunction for GST calculation in the isotropic case. The final time $T = 10\Delta t$, with $\Delta t = 10^{-2}$. Parameters are $R = 1$, $\lambda = -27$, $\tau_\xi = 5/3$, and $\phi_0 = 0.05$.*

We perform similar calculations, however this time we include anisotropic viscosity in the model. Based on the linear stability analysis in [23], and the results of the benchmark calculation in section 4, we see optimal growth of approximately $15 - 20^\circ$ to the shear plane. The parameters in these calculations were taken to be $R = 1$, $\lambda = -27$, $\tau_\xi = 5/3$, $\phi_0 = 0.05$ and the grid resoltuion was $100(i) * 50(j)$ grid cells. The size of the time-step is $\Delta t = 10^{-2}$, and the final time is $T = 10\Delta t$. We then used dolfin-adjoint to call the 30 largest singular values, and the associated eigenfunctions.

Refering to Figure 9, we see that for certain sequences of eigenfunctions, the growth rates are similar and the eigenfunctions qualitatively similar. This repetition is presumably a result of the error that arises from the periodic boundary conditions, which causes some asymmetry in the magnitude of the porosity in the bands, relative to position along the domain. We therefore focus our attention on eigefunctions that are distinctly different. Figure 8 shows

the 0th, 4th and 6th eigenfunctions, respectively, for the GST calculation with $T = 10\Delta t$. These figures show perturbations that are porosity bands oriented at approximately 15° to the plane of shear. This is an encouraging result, as it corresponds both with the numerical simulations and the linear stability analysis in [23]. Figure 8 shows that the growth of the bands is dependent on the wavelength, with Figure 8**a** showing the optimal wavelength.

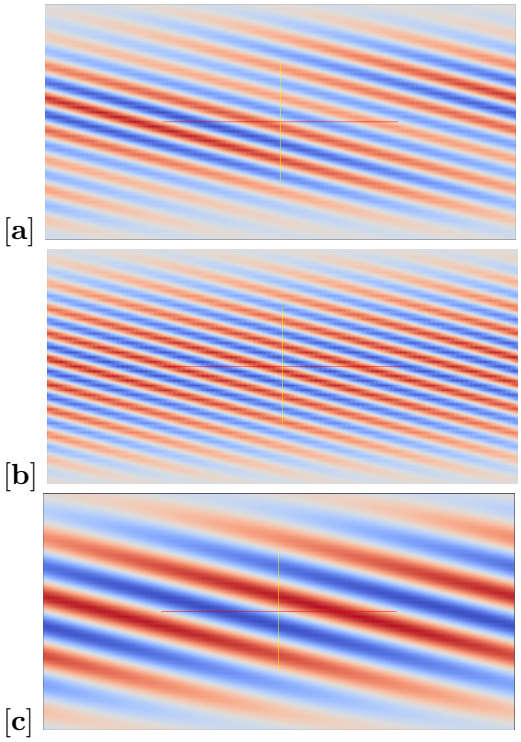

Figure 8: *Selection of eigenfunctions from a GST calculation for a propagator of* $T = 10\Delta t$, $\Delta t = 10^{-2}$, *and an initial condition of constant porosity* $\phi_0 = 0.05$ *throughout domain. The parameters are* $\lambda = -27$, $R = 1$, τ_ξ *and no diffusion. The mesh resolution is* $100(i) * 50(j)$ *grid cells. (**a**) shows the 0th eigenfunction, (**b**)the 4th eigenfunction and (**c**) the 6th eigenfunction of this calculation.*

Looking at higher eigenfunctions, we see some emergent patterns. Figures 10**a** and 10**b** exhibit a region of reduced porosity half way up the domain and spanning the whole width. This region of reduced porosity seems to concentrate melt into regions within the bands, leading to a higher rates of growth within localised regions of melt. Another explanation for this "splitting" regions is to maintain the bands at a lower angle as they are sheared by the background flow. Figures 10**c**, 10**d** and 10**e** show a similar pattern but with two regions of reduced porosity, spaced equally up the height of the domain.

As a further experiment, the same GST calculation for $T = 10\Delta t$ was performed, but this time taking the compaction length to be $R = 0.1$. The 0th eigenfunction is shown in Figure 11, and has a growth rate of 1.5636, compared to a growth rate of 1.6084 when $R = 1.0$. From Figure 11 we see that the optimal perturbation prefers a smaller wavelength for a smaller compaction length.

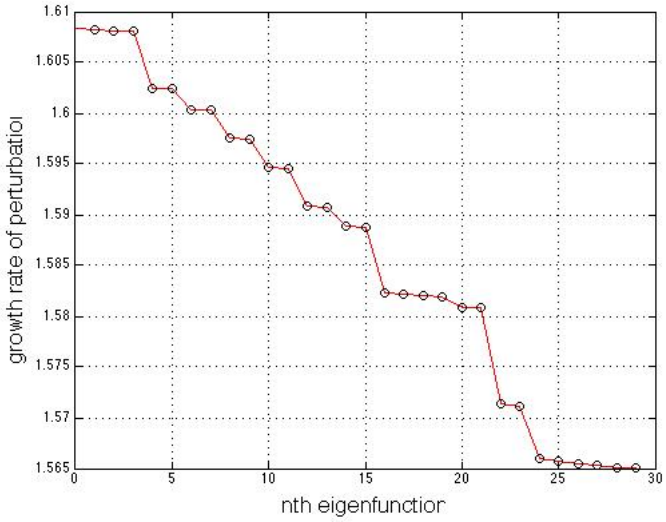

Figure 9: *Graph showing the growth rates for the 30 most optimally growing perturbations to a base state of* $\phi_0 = 0.05$. *The resolution for these GST calculations was 100(i)*50(j) grid cells and* $T = 10\Delta t$, *where* $\Delta t = 10^{-2}$.

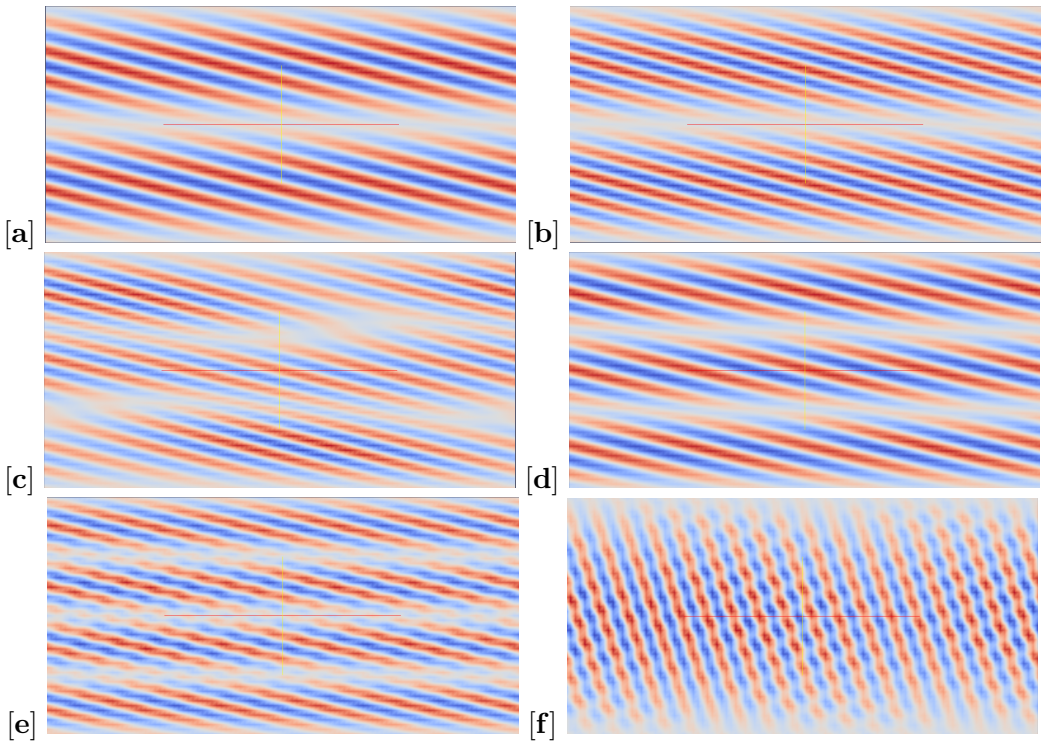

Figure 10: *Higher eigenfunctions for GST calculation with* $T = 10\Delta t$, $\Delta t = 10^{-2}$. *Parameters are* $\lambda = -27$, $R = 1$, τ_ξ, $\alpha = 2$, $\Theta = \pi/4$ *with mesh resolution of* $100(i) * 50(j)$ *grid cells.* ***(a)-(f)*** *correspond to the 8th, 10th, 16th, 20th, 24th and 28th eigenfunctions, respectively.*

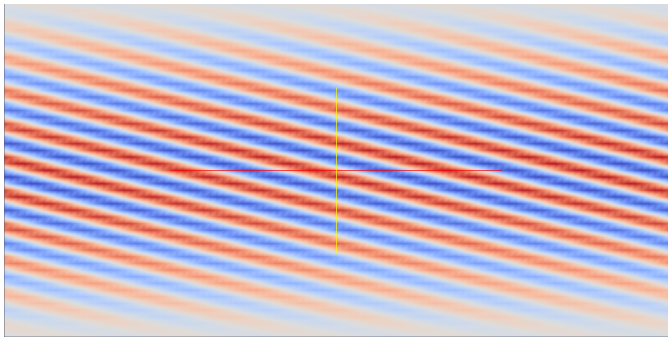

Figure 11: *0th eigenfunction for GST calculation for a smaller compaction length of* $R = 0.1$*, with anisotropic viscosity. The final time* $T = 10\Delta t$*, with* $\Delta t = 10^{-2}$*. Other parameters are* $\lambda = -27$*,* $\tau_\xi = 5/3$*,* $\alpha = 2$ *and* $\Theta = \pi/4$*. The mesh resolution is* $100(i) * 50(j)$ *grid cells.*

5.4 Caching Factorizations

As an aside, we take this opportunity to point out the computational cost associated with the GST calculation, as this can involve up to hundreds of iterations of tangent-linear and adjoint solves. This does restrict the resolution at which we can use GST. One way to help aleviate some of these issues is by caching the factorizations of the linearised operators. This caching exploits the similarity of the prognostic operators in the GST calculation by storing and reusing these factorisations over many tangent-linear and adjoint solves. The approach is detailed in [4].

Whilst this approach can greatly reduce the computation time, the issue with this caching is the severe memory cost associated with it. This is particularly true for nonlinear time-dependent problems. Possible tweaks to help with the memory cost are to use a Cholesky factorisation instead of an LU factorisation, and to use MUMPS out-of-core to compute the factors in RAM and store them on disk. For $T = 100\Delta t$, exceeding a resolution of $60(i)*30(j)$ requires more memory than is available (this is using a machine with 16GB memory).

5.5 Secondary instabilities

A robust observation from the experiments [6] is the formation of a network of channels between low angle porosity bands. It is possible to interpret this network of channels as a secondary perturbation, which acts to maintain the low angle bands.

A natural extension of the previous analysis would be to try and identify these "secondary" instabilities. This is to say that; given an optimal perturbation (over a time window $[0,\ T_1]$) that has been run forward to some final state u_{T_1}, what is the perturbation to this final state that will grow optimally over the time window $[T_1,\ T_2]$? Taking an optimal eigenfunction, such as in Figure 12**a**, and running it forward gives something similar in profile to Figure 12**b**. Peforming a GST calculation with this as an initial condition, for a propagator defined for $T = 10\Delta t$, gives the optimal eigenfunction shown in Figure 13**a**. The profile of this secondary perturbation is also $15 - 20^\circ$ bands.

To see the evolution of this perturbation, we superimpose it onto the initial condition, after

multiplying it by a scalar $\epsilon \ll 1$. This is then run forward in time. Figures 13**b**-13**g** show the output of this simulation. The small perturbation in Figure 13**a** shows the formation of channels between adjacent bands. These channels grow to re-distribute the melt in the high angle bands into low angle bands. Although this example is a simplified analogue of what is seen in experiments [6], it demonstrates the basic mechanism that brings the rotated bands back to the optimally growing state, i.e low angle bands.

A further observation to note is that the initial state (with added perturbation) in Figure 13**a** is similar to the 28-th eigenfunction in Figure 10**f**. This suggests that the higher eigefunctions of the original GST calculation are picking out secondary instabilities of the optimal eigenfunction. Another explanation for this observation is that there is a optimal growth rate for bands at approximately 75° to the shear plane (as shown in Figure 5), and it is possible that these higher angle bands are produced as result of this in 10**f**.

It is still an open question as to how GST can identify secondary instabilies that form the network of bands seen in [6].

Having considered the case of anisotropic viscosity for two-phase flow in simple shear, we extend the previous methods to the two-dimensional parallel plate Poiseuille flow problem, as presented in Katz/Takei (2012) [23]. This is discussed in the next section.

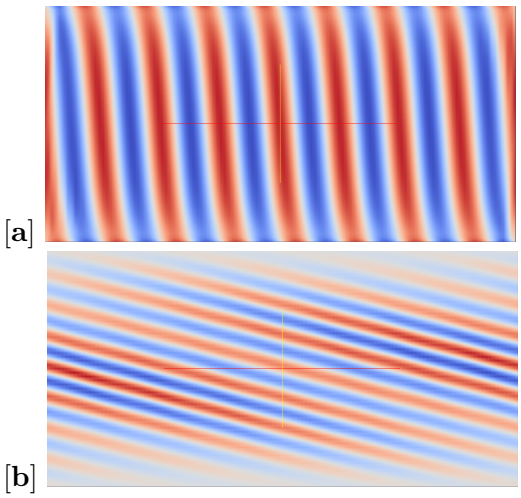

Figure 12: *(**a**): Initial porosity profile at t=0, ϕ_0. (**b**): Optimal perturbation from GST for $T = 10$, $\Delta t = 10^{-2}$: $\delta\phi_0$.*

6 2-D Poiseuille Flow

We now present an application of generalised stability theory to the two-dimensional Poiseuille flow problem, in a Cartesian geometry. In this set-up, the flow is driven by gravity in the negative y-direction, sandwiched between two parallel plates. To model this, we follow the approach in [23] by considering a domain that spans half of the distance between the fixed impermeable plates. The flow profile is assumed to be parabolic, so we impose a symmetry condition at $x = 0$. A sketch of the set-up is given in Figure 14.

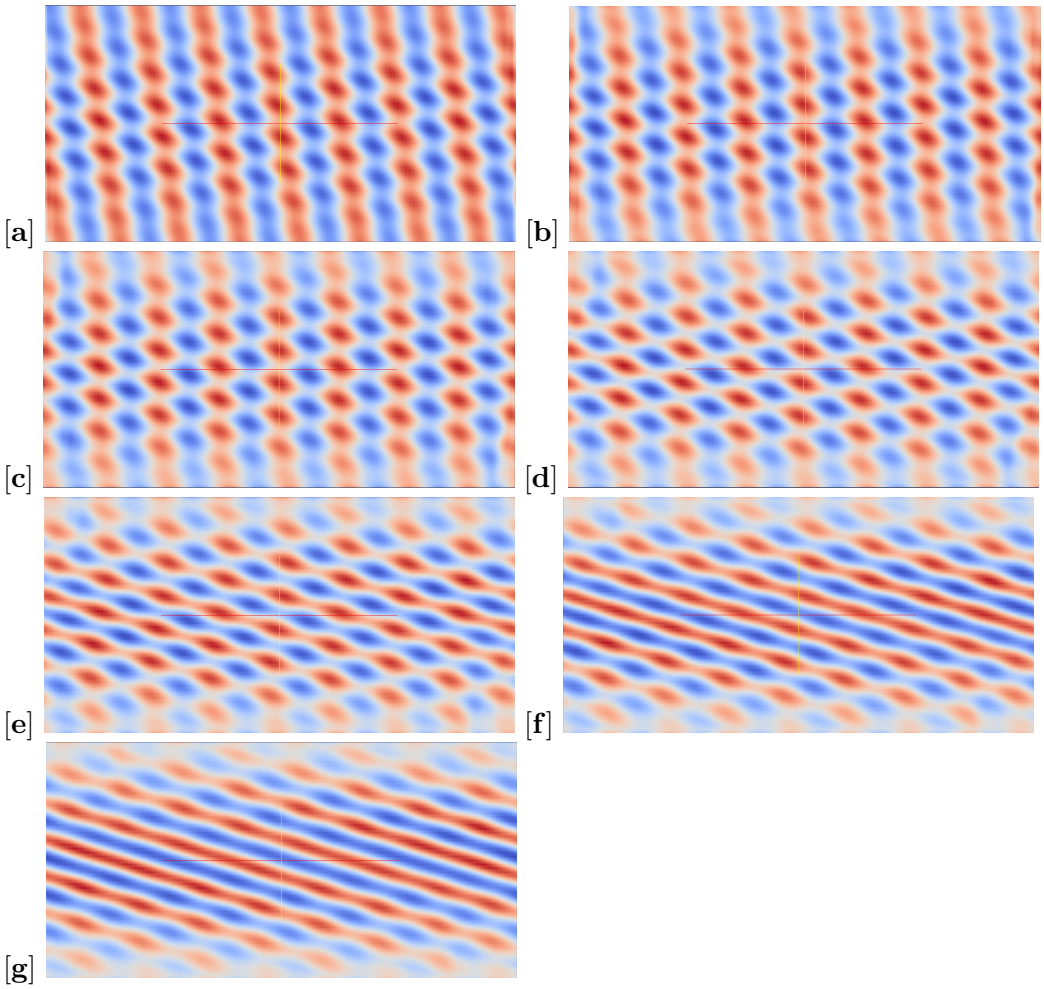

Figure 13: *(**a**): Initial condition given by $\phi_0 + \delta\phi_0$. (**b**)-(**g**) show snapshots of the evolution of the initial condition for intervals of $T = 10\Delta t$, $\Delta t = 10^{-2}$.*

6.1 Governing equations and boundary conditions

The equations for Poiseuille flow are similar to simple shear, except they include a gravity term. As before, on eliminating the liquid viscosity $\mathbf{v}^L$ and nondimensionalising, we have that

$$\frac{\partial \phi}{\partial \tau} = \nabla \cdot [(1-\phi)\mathbf{V}] \tag{88}$$

$$\nabla \cdot \mathbf{V} = \frac{R^2}{\tau_\xi + \frac{4}{3}} \nabla \cdot \left[(\frac{\phi}{\phi_0})^n (\nabla P - \mathbf{g}) \right] \tag{89}$$

$$P_{,i} = (C_{ijkl}\dot{\epsilon}_{kl})_{,j} + g_i, \tag{90}$$

where $\mathbf{g}$ is a unit vector pointing in the direction of gravity, which we take to be in the negative y-direction (see Figure 14). We assume periodic boundary conditions at the sides of the domain (in the y-direction). The boundary conditions at $x = H$ are no-slip, and a symmetry condition imposed at $x = 0$. The boundary conditions are:

$$\mathbf{V} = \mathbf{0}, \text{ for } x = H \qquad \mathbf{V} \cdot \mathbf{i} = 0,\ \partial_x P = 0,\ \partial_x(\mathbf{V} \cdot \mathbf{j}) = 0, \text{ for } x = 0 \tag{91}$$

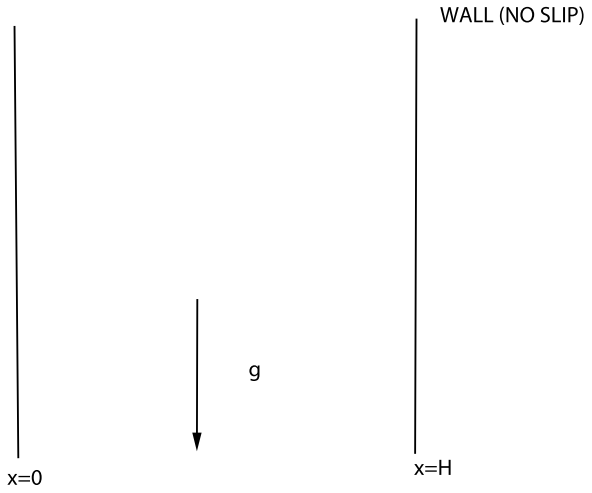

Figure 14: *Schematic of domain for Poiseuille flow. The right boundary at $x = H$ is an impermeable boundary with no-slip boundary conditions, and the left boundary $x = 0$ has a symmetry condition imposed on it. Gravity is taken to be in the positive x-direction, and is normalised so that $\mathbf{g} = -\mathbf{j}$.*

In the following we will explicitly refer to the Neumann boundary as the boundary $x = 0$, which will be denoted by Γ_N.

6.2 Weak Variational Formulation

There are parts of this derivation that are similar to the previous weak formulations, except that now there is a Neumann boundary condition at $x = 0$.

We start with

$$\nabla P - \mathbf{g} = \nabla \cdot \eta \left(\nabla \mathbf{V} + \nabla \mathbf{V}^T \right) + \nabla \left[\left(\xi - \frac{2}{3}\eta \right) \nabla \cdot \mathbf{V} \right]. \tag{92}$$

Multiplying through by a test function $\mathbf{U} \in H^1_{E0}(\Omega)$, integrating over the domain and applying Gauss' Theorem, the left hand side becomes

$$-\int_\Omega \epsilon(\mathbf{U}) : \eta \left(\nabla \mathbf{V} + \nabla \mathbf{V}^T \right) \mathrm{d}x + \int_{\Gamma_N} (\eta \left(\nabla \mathbf{V} + \nabla \mathbf{V}^T \right) \cdot \mathbf{n}) \cdot \mathbf{U} \mathrm{d}s + \int_\Omega \mathbf{U} \cdot \nabla \left[\left(\xi - \frac{2}{3}\eta \right) \nabla \cdot \mathbf{V} \right] \mathrm{d}x, \tag{93}$$

Where $\epsilon(\mathbf{U})$ is the symmetric gradient of $\mathbf{U}$. The right hand side just becomes

$$\int_\Omega \mathbf{U} \cdot \nabla P \mathrm{d}x - \int_\Omega \mathbf{U} \cdot \mathbf{g} \mathrm{d}x. \tag{94}$$

This can be written in the form

$$-\int_\Omega (\nabla \cdot \mathbf{U}) P \mathrm{d}x - \int_\Omega \mathbf{U} \cdot \mathbf{g} \mathrm{d}x. \tag{95}$$

Similarly, the third term in equation (93) becomes

$$-\int_\Omega \left(\xi - \frac{2}{3}\eta\right)(\nabla \cdot \mathbf{V})(\nabla \cdot \mathbf{U})\mathrm{d}x + \int_{\Gamma_N} \left(\xi - \frac{2}{3}\eta\right)(\nabla \cdot \mathbf{V})\mathbf{U} \cdot \mathbf{n} \mathrm{d}s \tag{96}$$

The normal to the boundary at $x = 0$ is $\mathbf{n} = \mathbf{i}$. In this case we have that

$$(\eta\left(\nabla \mathbf{V} + \nabla \mathbf{V}^T\right) \cdot \mathbf{n}) = \eta(2\partial_x u,\ \partial_x v + \partial_y u). \tag{97}$$

The boundary conditions at $x = 0$ state that $\partial_x v = 0$, and that $u = 0$ (u and v are defined by $\mathbf{V} = (u,\ v)$). The fact that u is constant on $x = 0$ implies that $\partial_y u = 0$ on Γ_N. The above then reduces to

$$(\eta\left(\nabla \mathbf{V} + \nabla \mathbf{V}^T\right) \cdot \mathbf{n}) = \eta(2\partial_x u,\ 0). \tag{98}$$

We now turn our attention to the anisotropic part of the stress tensor. This will be in the form of a second rank tensor; however, as there is not as "neat" a form for the anisotropic part as there is for the isotropic part, we revert to index notation. The strain rate tensor on Γ_N will be given by If we were to include the anisotropic part of the stress tensor in equation (90), it would be of the form

$$-(\alpha\eta a_{i1}a_{j1}a_{k1}a_{l1}\dot{\epsilon}_{kl})_{,j} \tag{100}$$

As $\dot{\epsilon}_{12}$ and $\dot{\epsilon}_{21}$ vanish on the boundary, we only consider terms including $\dot{\epsilon}_{11}$ and $\dot{\epsilon}_{22}$. Multiplying (100) through by a test function $\mathbf{U} \in H^1_{E0}(\Omega)$ and integrating over the domain gives

$$-\int_\Omega U_i(\alpha\eta a_{i1}a_{j1}a_{k1}a_{l1}\dot{\epsilon}_{kl})_{,j}\ \mathrm{d}x_i. \tag{101}$$

We define a second rank tensor $\mathbf{\Sigma}$ such that $(\mathbf{\Sigma})_{ij} = \alpha\eta a_{i1}a_{j1}a_{k1}a_{l1}\dot{\epsilon}_{kl}$. Integrating (101) by parts and applying Gauss' theorem gives

$$\int_\Omega \epsilon(\mathbf{U}) : \mathbf{\Sigma} \mathrm{d}x - \int_{\Gamma_N} (\mathbf{\Sigma} \cdot \mathbf{n}) \cdot \mathbf{U} \mathrm{d}s. \tag{102}$$

As $\mathbf{n} = \mathbf{j}$, we need only consider the entries $(\mathbf{\Sigma})_{21}$ and $(\mathbf{\Sigma})_{11}$.

$$(\mathbf{\Sigma})_{21} = \alpha\eta a_{21}a_{11}a_{k1}a_{l1}\dot{\epsilon}_{kl} \tag{103}$$

$$= \alpha\eta a_{21}a_{11}a_{11}a_{11}\dot{\epsilon}_{11} + \alpha\eta a_{21}a_{11}a_{21}a_{21}\dot{\epsilon}_{22} \tag{104}$$

$$= \alpha\eta cos^3\Theta sin\Theta\partial_x u + \alpha\eta cos\Theta sin^3\Theta\partial_y v \tag{105}$$

Similarly, $(\mathbf{\Sigma})_{11}$ is given by

$$(\mathbf{\Sigma})_{11} = \alpha\eta cos^2\Theta sin^2\Theta\partial_x u + \alpha\eta cos^4\Theta\partial_y v. \tag{106}$$

Hence we have that the boundary integral in (102) is

$$-\int_{\Gamma_N} \alpha\eta((cos^2\Theta sin^2\Theta + cos^3\Theta sin\Theta)\partial_x u + (cos\Theta sin^3\Theta + cos^4\Theta)\partial_y v,\ 0) \cdot \mathbf{U} \mathrm{d}s \tag{107}$$

Combining both the weak forms for the anisotropic and isotropic parts of the stress tensor gives us that

$$
\begin{aligned}
-\int_\Omega (\nabla\cdot\mathbf{U})P\mathrm{d}x - \int_\Omega \mathbf{U}\cdot\mathbf{g}\mathrm{d}x = -\int_\Omega \epsilon(\mathbf{U}) : \eta\left(\nabla\mathbf{V} + \nabla\mathbf{V}^T\right)\mathrm{d}x + \int_{\Gamma_N} \eta(0,\, 2\partial_y v)\cdot\mathbf{U}\mathrm{d}s \\
-\int_\Omega \left(\xi - \frac{2}{3}\eta\right)(\nabla\cdot\mathbf{V})(\nabla\cdot\mathbf{U})\mathrm{d}x + \int_{\Gamma_N}\left(\xi-\frac{2}{3}\eta\right)(\nabla\cdot\mathbf{V})\mathbf{U}\cdot\mathbf{n}\mathrm{d}s \\
+\int_\Omega \epsilon(\mathbf{U}) : \mathbf{\Sigma}\mathrm{d}x - \int_{\Gamma_N}\alpha\eta\mathbf{F}\cdot\mathbf{U}\mathrm{d}s, \quad (108)
\end{aligned}
$$

where $\mathbf{F} = ((cos^2\Theta sin^2\Theta + cos^3\Theta sin\Theta)\partial_x u + (cos\Theta sin^3\Theta + cos^4\Theta)\partial_y v,\ 0)$.

Now we consider the equation

$$
\nabla\cdot\mathbf{V} = \frac{R^2}{\tau_\xi + \frac{4}{3}}\nabla\cdot\left[(\frac{\phi}{\phi_0})^n(\nabla P - \mathbf{g})\right] \quad (109)
$$

We multiply the above through by a test function $Q \in L^2(\Omega)$ and integrate over the domain. This gives

$$
\int_\Omega Q\nabla\cdot\mathbf{V}\mathrm{d}x = \int_\Omega Q\frac{R^2}{\tau_\xi + \frac{4}{3}}\nabla\cdot\left[(\frac{\phi}{\phi_0})^n(\nabla P - \mathbf{g})\right]\mathrm{d}x. \quad (110)
$$

Rewriting the RHS of (110) gives us that

$$
\int_\Omega Q\nabla\cdot\mathbf{V}\mathrm{d}x = \int_\Omega \frac{R^2}{\tau_\xi + \frac{4}{3}}\nabla\cdot\left[Q(\frac{\phi}{\phi_0})^n(\nabla P - \mathbf{g})\right]\mathrm{d}x - \int_\Omega \frac{R^2}{\tau_\xi + \frac{4}{3}}\nabla Q\cdot\left[(\frac{\phi}{\phi_0})^n(\nabla P - \mathbf{g})\right]\mathrm{d}x. \quad (111)
$$

Applying Gauss' theorem to the above gives

$$
\int_\Omega Q\nabla\cdot\mathbf{V}\mathrm{d}x = \int_{\Gamma_N} \frac{R^2}{\tau_\xi + \frac{4}{3}}\left[Q(\frac{\phi}{\phi_0})^n(\nabla P - \mathbf{g})\right]\cdot\mathrm{d}\mathbf{s} - \int_\Omega \frac{R^2}{\tau_\xi + \frac{4}{3}}\nabla Q\cdot\left[(\frac{\phi}{\phi_0})^n(\nabla P - \mathbf{g})\right]\mathrm{d}x. \quad (112)
$$

On Γ_N we have the condition that $\partial_x P = 0$. This causes the boundary term in (112) to vanish, and so we are left with

$$
\int_\Omega Q\nabla\cdot\mathbf{V}\mathrm{d}x = -\int_\Omega \frac{R^2}{\tau_\xi + \frac{4}{3}}\nabla Q\cdot\left[(\frac{\phi}{\phi_0})^n(\nabla P - \mathbf{g})\right]\mathrm{d}x. \quad (113)
$$

Combining (113) and (108), we have the weak variational formulation for the "Stokes" equations: *Find a* $V \in H^1_E$ *and a* $P \in L^2(\Omega)$ *such that:*

$$
\begin{aligned}
-\int_\Omega (\nabla\cdot\mathbf{U})P\mathrm{d}x - \int_\Omega \mathbf{U}\cdot\mathbf{g}\mathrm{d}x + \int_\Omega \epsilon(\mathbf{U}) : \eta\left(\nabla\mathbf{V} + \nabla\mathbf{V}^T\right)\mathrm{d}x - \int_{\Gamma_N}\eta(0,\, 2\partial_y v)\cdot\mathbf{U}\mathrm{d}s \\
+\int_\Omega \left(\xi - \frac{2}{3}\eta\right)(\nabla\cdot\mathbf{V})(\nabla\cdot\mathbf{U})\mathrm{d}x - \int_{\Gamma_N}\left(\xi-\frac{2}{3}\eta\right)(\nabla\cdot\mathbf{V})\mathbf{U}\cdot\mathbf{n}\mathrm{d}s \\
-\int_\Omega \epsilon(\mathbf{U}) : \mathbf{\Sigma}\mathrm{d}x + \int_{\Gamma_N}\alpha\eta\mathbf{F}\cdot\mathbf{U}\mathrm{d}s - \int_\Omega Q\nabla\cdot\mathbf{V}\mathrm{d}x - \int_\Omega \frac{R^2}{\tau_\xi + \frac{4}{3}}\nabla Q\cdot\left[(\frac{\phi}{\phi_0})^n(\nabla P - \mathbf{g})\right]\mathrm{d}x = 0, \\
\forall\mathbf{U} \in H^1_{E0} \text{ and } \forall Q \in L^2(\Omega). \quad (114)
\end{aligned}
$$

The weak formulation of the advection equation is identical to previous analysis.

6.3 Forward Model

The weak formulation is used with a spatial discretisation using Taylor-Hood P2/P1 elements to construct a finite element approximation to the system of equations (88)-(90). The mesh resolution in the simulations was $30(i) * 60(j)$ grid cells, and the time-step was taken to be $\Delta t = 10^{-2}$. Figure 15 shows snapshots from a series of different simulations. The simulations are run for different compactions lengths $R = 0.1$ and $R = 1$ and for different magnitudes of anisotropy α. The initial perturbation is the random variable $\mathbf{X} = \phi_0 + \mathbf{Y}$, where $\mathbf{Y}$ is a random Gaussian number taken from the interval $(-0.01,\ 0.01)$. Gravity is in the negative y-direction for these images.

As described in [23], Poiseuille flow with anisotropic viscosity has three distinct modes of segregation. The first is the gravitional body force which drives the flow. This acts on both phases, and tends to drive the liquid phase more rapidly than the solid phase. The background deformation field of the solid phase simultaneously drives two other modes of segregation. The first is localisation into high-porosity bands. For a sufficiently small section of the domain, one can view the solid flow approximately as simple shear. The second mode is liquid segregation over the entire domain. The liquid moves up the stress gradient towards a region of higher stress, which is located at the no-slip boundary. We can refer to these two modes seperately: the latter we will refer to as a "base-state" flow. This is because the behaviour is irrespective of perturbations to the background Poiseuille flow. In the linear analysis of the full equations, these two modes are treated seperately, and their growth rates can be calculated. In numerical solutions, however, the two modes are tracked simulatenously to capture the full evolution of the porosity.

For $\alpha = 0$ and $\alpha = 2$ we see the consistent alignment of high porosity bands at the wall, for both compaction lengths $R = 1$ and $R = 0.1$. For $\alpha = 1.5$ we see more complicated behaviour: as is described in [8], the porosity features are aligned at angles greater than $45°$, however these segments of high porosity are placed sequentially along lines that are less than $45°$ to the shear plane. According to [8], the behaviour when $\alpha = 1.5$ is similar to the simple shear simulations. The results of these simulations appear to replicate the simulations produced in recent work by Katz, so the validity of the code is can be considered reasonable.

Using the code used to run the previous simulations, we can use generalised stability theory to determine the optimally growing perturbations to a initial uniform porosity. This is described in the next section.

6.4 Generalised Stability Theory

We apply generalised stability theory to the 2-D Poiseuille flow problem. The initial condition is taken to be uniform porosity throughout the domain, with $\phi_0 = 0.05$. The parameters are taken to be $R = 1$, $\lambda = -27$, $\tau_\xi = 5/3$, $\alpha = 2$ and $\Theta = \pi/4$. The mesh resolution is taken to be $50(i) * 100(j)$ grid cells, and the time-step is $\Delta t = 10^{-3}$. The time window over which we hope to identify optimally growing porosity perturbations is $T = 10\Delta t$.

The 0th eigenfunction is shown in Figure 16. Its associated growth rate is 1.1343. The perturbation clearly show a banded structure, with a low angle orientation relative to the wall. Comparing with Figure 15**a**, which also has $R = 1$ and $\alpha = 2$, there is a resembelance

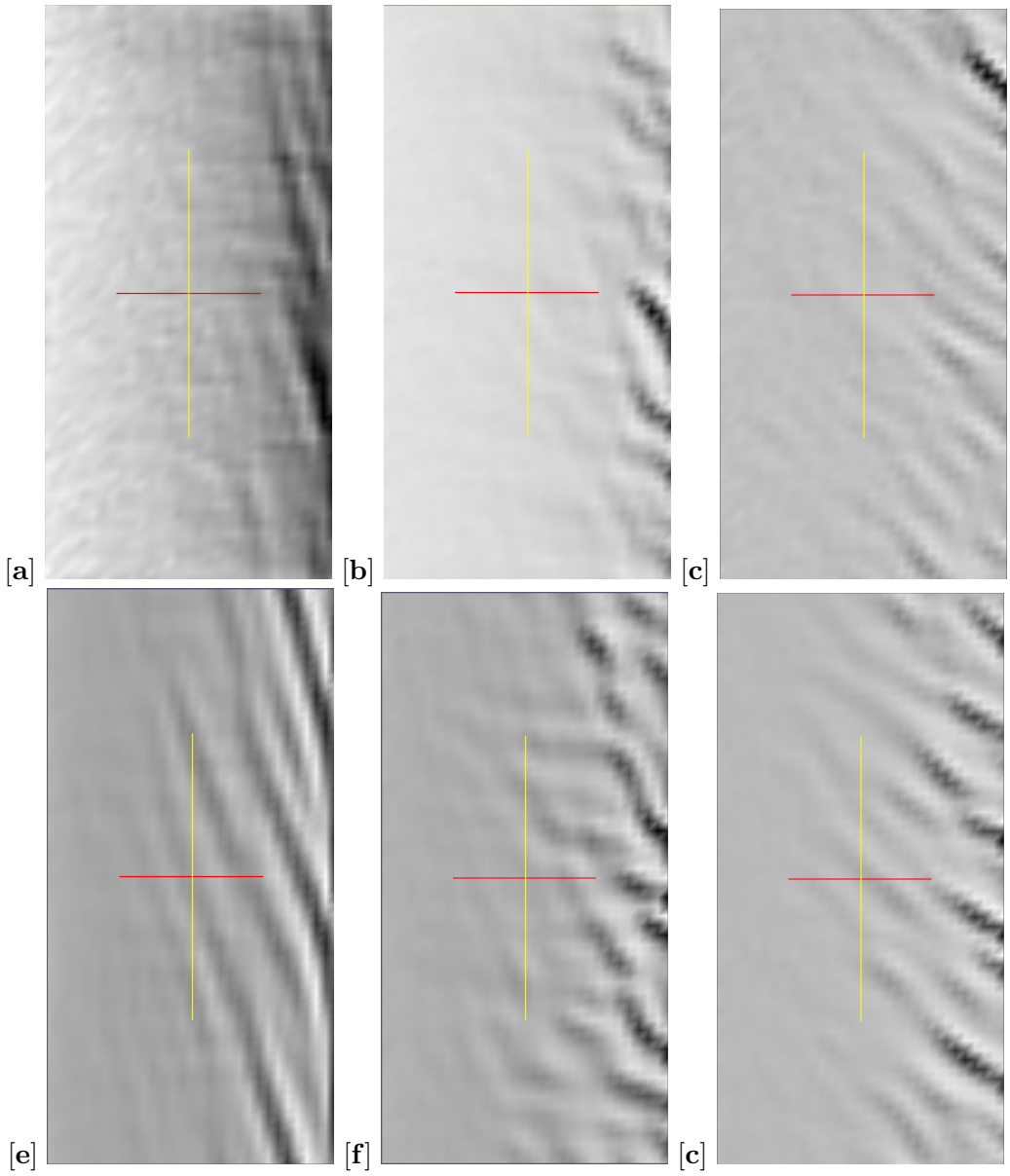

Figure 15: *Results of simulated porosity for 2D Poiseuille flow. (**a**) shows the porosity at time T=0.2, with R=1, $\alpha = 2$. (**b**) is for T=0.4, R=1, $\alpha = 1.5$ and (**c**) is for T=0.53, R=1, $\alpha = 0$. (**d**) is for time T=1.0, R=0.1, $\alpha = 2$. (**e**) is for T=1.0, R=0.1, $\alpha = 1.5$ and (**f**) is for time T=1.0, R=0.1, $\alpha = 0$*

in the pattern that forms near the wall. The GST calculation appears to correctly predict the formation of bands as an optimally growing perturbation.

We now move to extend the code to model the problem of a simple shear two-phase flow around a rigid inclusion.

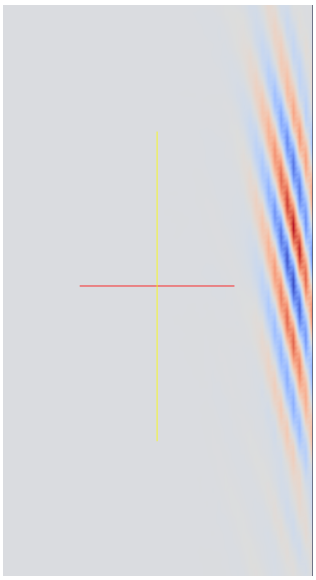

Figure 16: *0th eigenfunction with* $T = 10\Delta t$, $\Delta t = 10^{-3}$. *Grow rate of perturbation is* 1.1343.

7 Compaction around a rigid cylinder

7.1 Background

This problem is based on experiments performed by Qi and Kohlstedt, which are detailed in [1]. In these experiments a fine-grained, partially molten aggregate of olivine and basalt is derformed around an approximately rigid, olivine sphere. A two-phase distribution of solid and melt then forms around the inclusion. After a certain strain, the resulting physical state can be quenced and observed. One particular observation is that a perturbation to the pressure field gives rise to a 4-fold symmetry of low and high pressure regions, or "pressure shadows". This pressure perturbation results in melt-enriched and melt-depleted regions, which are themselves perturbations to the porosity field.

An interesting observation in these experiments is the emergence of porosity bands. There has been extensive theoretical work [12] on the study of the formation of pressure shadows around a rigid sphere in a two-phase compactable flow. However, there is little that documents the emergence of this instability, and quantifies how these two modes of segregation compete with one another; that is, the formation of pressure shadows and porosity bands. The framework of generalised stability theory stands out as a potentially fruitful way of studying these two modes simultaneously.

7.2 Code Benchmarking

To benchmark the code, we refer to the analytical solution presented in [15]. This analytical result gives the instantaneous solution to the compaction equations, based on the model in [11], which is obtained by the use of Papkovich-Neuber potentials. Away from the inclusion the velocity field can be described by $\mathbf{V}_\infty = \mathbf{E} \cdot \mathbf{x}$, where $\mathbf{E}$ is the symmetric strain tensor

given by

$$\mathbf{E} = \begin{bmatrix} 0 & \gamma/2 \\ \gamma/2 & 0 \end{bmatrix}. \tag{115}$$

The governing equations are solved according to $\mathbf{v}_s = -\mathbf{V}_\infty$ on the inclusion boundary, along with $\frac{\partial P}{\partial n} = 0$. Here $\mathbf{v}_s$ is the velocity of the solid matrix. Following the analysis in [15], we obtain an analytical solution of the form

$$\mathbf{v}_s = \left(-\frac{4D}{r^2} + \frac{2FK_2(r)}{r^2}\right)\mathbf{E}\cdot\mathbf{x} + \left(-\frac{2C}{r^4} + \frac{8D}{r^6} - \frac{FK_3(r)}{r^3}\right)(\mathbf{x}\cdot\mathbf{E}\cdot\mathbf{x})\mathbf{x}, \tag{116}$$

$$P = \left(-\frac{4BC}{r^4} + \frac{FK_2(r)}{r^2}\right)\mathbf{x}\cdot\mathbf{E}\cdot\mathbf{x}. \tag{117}$$

In these solutions, $K_n(r)$ is the modified Bessel function of the second kind. The constants are determined by

$$B = \frac{1}{\tau_\xi + \frac{4}{3}}, \tag{118}$$

$$C = -\frac{a^4 K_2'(a)}{4BK_1(a) - a^2 K_2'(a)}, \tag{119}$$

$$D = \frac{a^4}{4} + \frac{4a^3 BK_2(a)}{4Bk_1(a) - a^2 K_2'(a)}, \tag{120}$$

$$F = \frac{8aB}{4BK_1(a) - a^2 K_2'(a)}. \tag{121}$$

In the above, a is defined to be the dimensionless radius of the cylinder, divided by the reference compaction length R. The compaction rate of the solution velocity can be written as

$$\nabla\cdot\mathbf{v}_s = \frac{FK_2(r)}{r^2}\mathbf{x}\cdot\mathbf{E}\cdot\mathbf{x}. \tag{122}$$

As a benchmark calculation we compute the L_2 norm of the velocity errors. To reduce the interference from the top and bottom boundaries on the cylinder, we prescribe a small radius $r = 0.025$. The height of the domain is taken to be $H = 2$. The errors in the i-th and j-th velocity components are 0.003807 and 0.004571, respectively. To validate the code further, the total torque on the boundary of the cylinder was computed at each time-step. This typically gives values of orders $10^{-18} - 10^{-16}$, which supports the claim that the boundary condition has been implemented correctly.

7.3 Forward Model

To simulate the flow around the cylindrical inclusion described in [1], we impose a circular impermeable boundary at the centre of the domain, with radius 0.1. As previously, the dimensions of the rectangular domain are 2×1. The inclusion is assumed to rotate with

the sense of shear - so in a clock-wise direction - and the boundary condition is given by the assumption of zero torque on the its boundary.

The results in the following sections refer only to the case where the stress tensor is isotropic - we will defer the inclusion of anisotropic viscosity to a later point. The images in Figure 17 are taken from a simulation with a mesh resolution of $100(i)*200(j)$ grid cells, and a time-step $\Delta t = 5 \times 10^{-3}$. The parameters are taken to be $\tau_\xi = 5/3$, $\lambda = -27$ and $R = 1.0$. The intial condition, ϕ_0, at each node takes the value of a random variable $\mathbf{X} = 0.05 + \mathbf{Y}$, where $\mathbf{Y}$ takes the value of random Gaussian distribution on the interval $(-\epsilon, \epsilon)$. In the present simulation the amplitude of the background noise perturbation ϵ was taken to be 10^{-3}. Further, we include a diffusion term with exponent $m = 3$.

The results of the porosity evolution simulation show an instantaneous 4-fold "lobing" effect around the surface of the cylinder, which are the result of pressure shadows. Figure 17**a** shows this instantaneous pressure shadow formation around the cylinder after a single time-step. Figures 17**b**-17**c** show the development of this simulation after 5 and 10 time-steps respectively. Once we reach $T = 10\Delta t$, there is little visible background noise, and the pressure shadows dominate the porosity profile in the domain. To see the further evolution of this forward model we refer to Figures 17**d**-17**i**. These figures show the gradual formation of melt-enriched bands. In this simulation, we can see that once the pressure shadow has formed, the melt-enriched regions nucleate the growth of bands. Figure 17**f** shows that eventually the bands grow to a critical point, at which they begin to deplete melt from the regions where the pressure shadows formed. Figures 17**g**-17**h** shows that this continued growth eventually causes the bands to "detach" from the cylinder completely, leaving a region of low porosity surrounding the inclusion. Furthermore, running the model forward for $T = 400\Delta t$, as seen in Figure 17**i**, we see that the two high-porosity bands converge to form one band that is centred in the domain.

The same simulation was run but instead taking the background noise perturbation of $\epsilon = 10^{-4}$. The simulation of this model gives similar results, except that the pressure shadows form even more quickly. To see whether the formation of the bands in Figure 17 are a result of the noise perturbation, we ran the same simulation but with a constant background porosity of $\phi_0 = 0.05$. In other words, we would like to determine whether or not the formation of bands over large strains is an instability.

Figure 18 shows the results of these no-noise simulations. It is clear form these images that porosity bands form tangentially to the boundary of the inclusion. Figure 18**a** shows a snapshot from a simulation with no noise perturbation but with diffusion $m = 3$, and Figure 18**b** shows a snapshot form a simulation with no noise and no diffusion. We note that Figure 18**a** shows the final time that the simulation runs until, as the after this point the Newton solver fails to converge. From this image it is therefore difficult to tell whether or not the bands detach entirely from the boundary.

Figure 18**b** shows a similar porosity profile, except that the bands that form are thinner, due to the lack of diffusion. However, the main problem is that without diffusion, the growth of the bands is not restricted, which results in porosities porosities >1 within the bands. The solution fails to converge after the snapshot shown in Figure 18**b**, with a maximum porosity value of 1.24.

The parameters are $R = 1$, $\lambda = -27$ and $\tau_\xi = 5/3$ in both of these simulations.

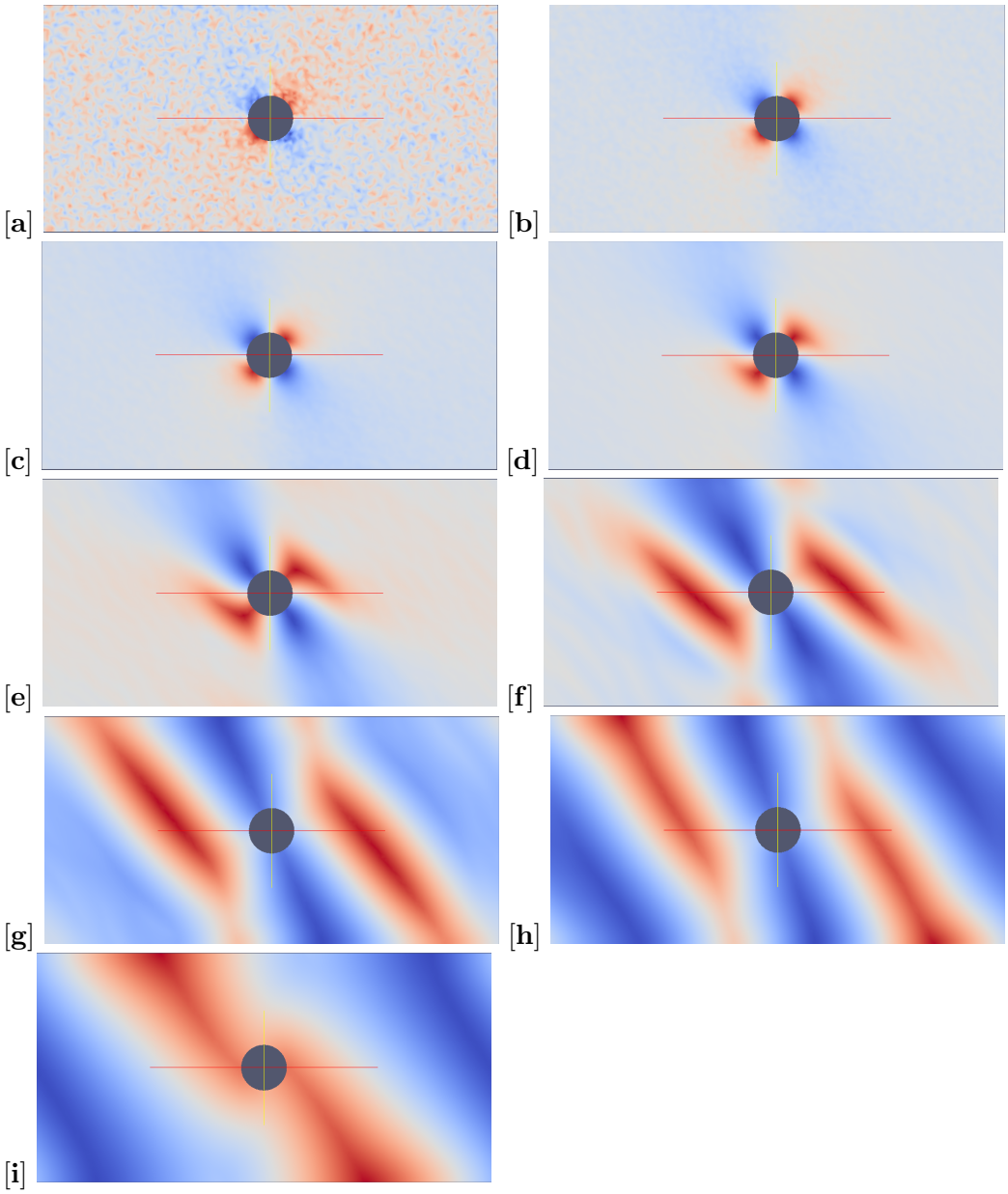

Figure 17: *Snapshots of porosity evolution for a forward run of the flow around a cylindrical inclusion, in the isotropic case.* ***(a)****:* $T = 1\Delta t$, $\Delta t = 10^{-3}$. *Diffusion coefficient* $m = 3$, $R = 1$, $\lambda = -27$, $\tau_\xi = 5/3$, *noise perturbation amplitude* $\epsilon = 10^{-3}$. ***(b)*** *and* ***(c)*** *show snapshots after* $T = 5\Delta t$ *and* $T = 10\Delta t$ *time-steps, respectively.* ***(d)****-****(c)*** *show the snapshots after* $T = 25\Delta t$, $50\Delta t$, $100\Delta t$, $150\Delta t$, $200\Delta t$, $400\Delta t$ *time-steps, respectively.*

7.4 Harmonic Perturbation

As we are interested in the competing modes of melt segregation in this problem, it is useful to consider the effect of imposing porosity bands as an initial condition. An interesting question to ask is whether these bands will be dominated by the formation of pressure shadows, or

[**a**]

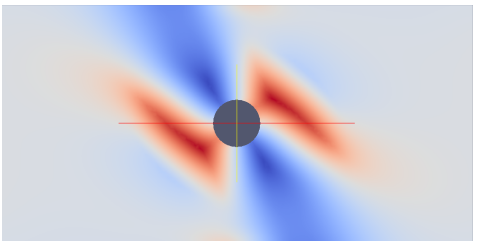

[**b**]

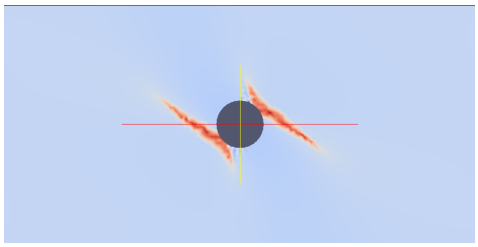

Figure 18: *(**a**): Forward run with initial uniform porosity $\phi_0 = 0.05$ (no noise perturbation). Final snapshot (before failure of convergence) at $T = 77\Delta t$, $\Delta t = 10^{-2}$. $m = 3$, $R = 1$, $\lambda = -27$, $\tau_\xi = 5/3$. The maximum porosity is 0.136. (**b**): Forward run with initial uniform porosity $\phi_0 = 0.05$ (no noise perturbation) and no diffusion term ($m = 0$). Final snapshot (before failure of convergence) at $T = 70\Delta t$, $\Delta t = 10^{-2}$. $R = 1$, $\lambda = -27$, $\tau_\xi = 5/3$. The maximum porosity is 1.24.*

vice versa. It is also important to determine what parameter regimes affect this. As a test we added an initial harmonic perturbation of the form $\phi = \phi_0 + \Psi \cos(k_0(x \sin(\theta_0) + y \cos(\theta_0)))$, where we take $k_0 = 8\pi$, $\theta_0 = \pi/4$, and $\Psi = 10^{-3}$.

Figure 19 show a run forward run of this model. Figure 19**a** shows the initial profile of this perturbation, and Figures 19**b**-19**c** show a gradual formation of pressure shadows around the inclusion. This growth is at the expense of the band that cuts through the centre of the inclusion. As the lobes develop, they feed melt into the bands adjacent to the the inclusion, therefore facilitating the further growth of these bands. Eventually we end up with a similar situation to what we have seen previously, where two bands tend to dominate the whole domain. The main conclusion of this experiment is to illustrate the point that if we impose bands on the domain, the bands will deplete melt from the melt-rich regions in the pressure shadows, causing further growth of bands at 45° to the shear plane.

7.5 Generalised stability theory

We use GST to comptue the SVD of the linearised propagator. As before, this will give us the optimal growing eigenfunctions, applied to some initial state, and their respective growth rates. For these calculations we take the initial state to be constant, uniform porosity throughout the domain with $\phi_0 = 0.05$. We consider optimally growing perturbations to this base state over a finite time $T = 5\Delta t$, where $\Delta t = 5 \times 10^{-3}$. The parameters for this simulation are $\tau_\xi = 5/3$, $\lambda = -27$, $R = 1$. Diffusion was also considered in this calculation, and the diffusion exponent was taken to be $m = 2$ (instead of $m = 3$). The mesh resolution was $200(i) * 100(j)$ grid cells.

The first 4 eigenfunctions are shown in Figure 20. These figures show a clear banding structure

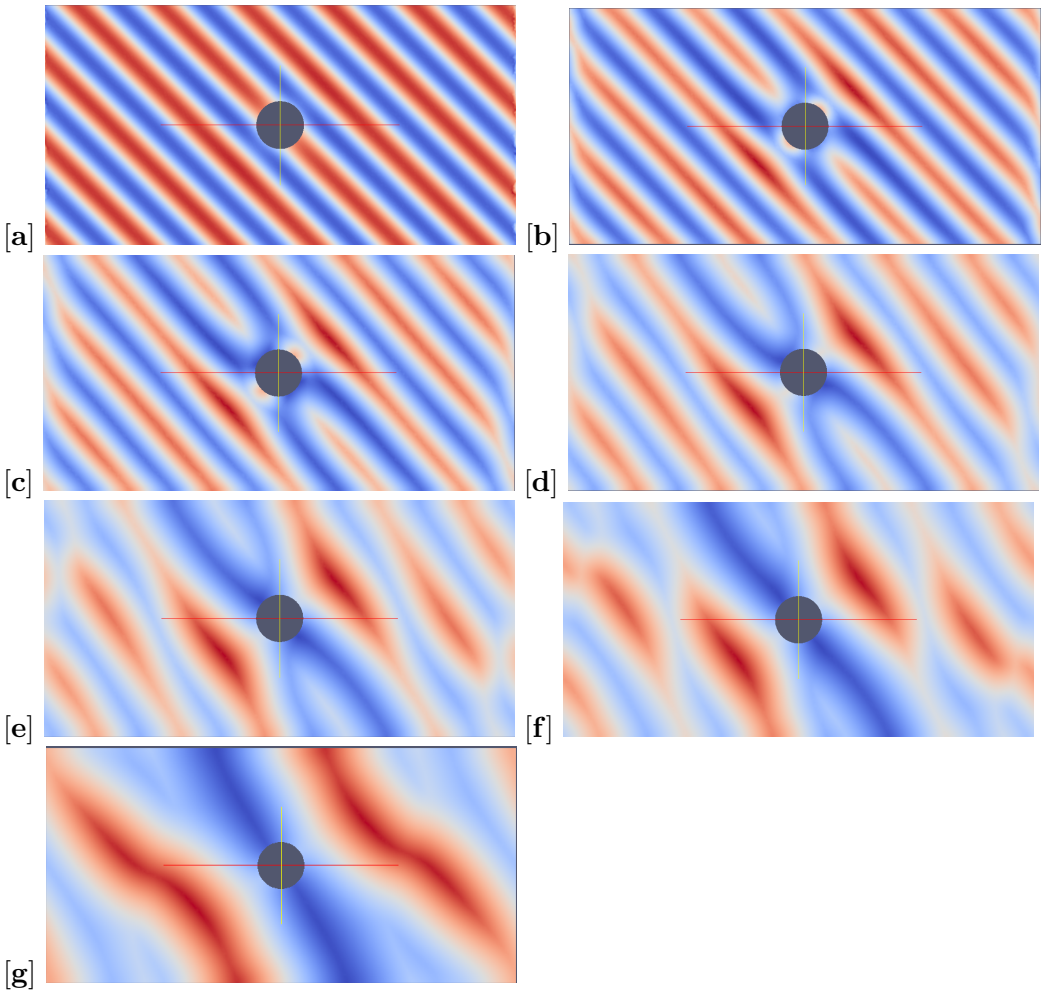

Figure 19: *Snapshots of porosity evolution for an initial harmonic perturbation. Parameters are* $\Delta t = 10^{-3}$. $\tau_\xi = 5/3$, $\lambda = -27$, $R = 1.0$, $m = 3$. *(**a**)-(**g**) show the evolved porosity field at time-steps* $T = 0$, $10\Delta t$, $25\Delta t$, $50\Delta t$, $75\Delta t$, $100\Delta t$ *and* $150\Delta t$, *respectively.*

in the 1st and 3rd quadrants around the cylinder. We interpret these results as saying that over this small time interval, the banded structure in these regions is the perturbation that grows optimally. Over time, however, the pressure shadows grow outwards and can swallow up these bands. This means that, after large strains with this perturbation applied, pressure shadows may still dominate.

We can also see how altering particular parameters affects the results from the GST calculation. A candidate parameter that determines the growth of pressure shadows versus the growth of bands is the bulk/shear viscosity ratio τ_ξ. The true value of constant is not known, although there is some work which predicts it to be 5/3 [21]. The same calculation is performed for $\tau_\xi = 10$, and the results are shown in Figure 21. In the case where $\tau_\xi = 10$, the bands do not extend in length as much as in the case where $\tau_\xi = 5/3$. Further if we consider the growth rates for the 0th eigenfunction we have a rate of 1.3579 when $\tau_\xi = 5/3$ and 1.1159 when $\tau_\xi = 10$. This suggests that where this instability forms, the rate that it emerges depends on the ratio τ_ξ. This preliminary calculation would suggest that as the ratio

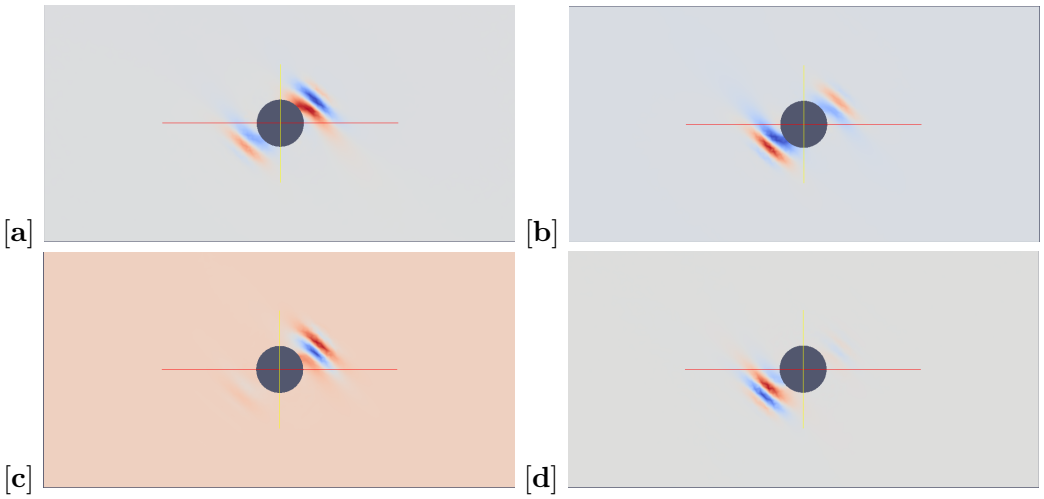

Figure 20: *Selection of eigenfunctions for a GST calculation with propagator* $T = 5\Delta t$, $\Delta t = 10^{-3}$. *Calculation is performed for an initial condition of uniform porosity* ($\phi_0 = 0.05$) *throughout the domain with parameters* $\tau_\xi = 5/3$, $\lambda = -27$, $R = 1.0$ *and diffusion coefficient* $m = 2$. (***a***)-(***d***) *show the 0th, 1st, 2nd and 3rd eigenfunctions, respectively. The respective growth rates of these perturbations are 1.3579, 1.3562, 1.3410 and 1.3400.*

of bulk to shear viscosity increases, so the growth of bands is reduced.

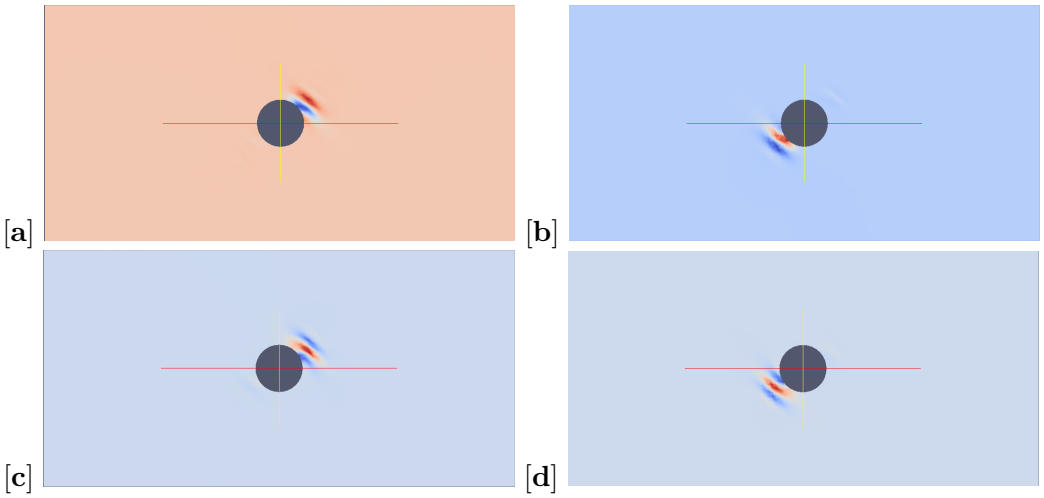

Figure 21: *Selection of eigenfunctions for a GST calculation with propagator* $T = 5\Delta t$, $\Delta t = 10^{-3}$. *This calculation is performed with the same parameters except this time with* $\tau_\xi = 10$. (***a***)-(***d***) *show the 0th, 1st, 2nd and 3rd eigenfunctions, respectively. The respective growth rates of these perturbations are 1.1159, 1.1145, 1.1083 and 1.1077.*

7.6 Anisotropic Viscosity

Next we considered adding anisotropic viscosity to the model. The assumption of fixed anisotropy is adopted with $\alpha = 2$ and $\Theta = \pi/4$. We ran the same forward model with a time-step of $\Delta t = 5 \times 10^{-3}$ and a mesh resolution of $400(i) * 200(j)$ grid cells. We note that there was no diffusion term used in this calculation. Other parameters are $R = 1$, $\lambda = -27$, $\tau_\xi = 5/3$, and $\phi_0 = 0.05$. The initial condition is a noise perturbation with noise amplitude $\epsilon = 10^{-3}$. Figure 22 shows the formation of pressure shadows, but not distributed symmetrically as in the isotropic case. In Figure 22(**d**) there is a region of very concentrated melt in regions to the left and right of the cylinder, and a longer melt-depleted region spanning from top to bottom.

Figure 23 shows the same simulation but with an added diffusion term. The exponent of the diffusion term is taken to be $m = 3$. There are notable differences between this simulation and the previous one, where there was no diffusion. These figures exhibit an initial formation of pressure shadows, which become "stretched" out to become parallel to the melt-dpleted channel cutting vertically through the centre of the domain. In Figures 23(**c**)-23(**e**) we see separate regions of enriched melt forming off the pressure shadows. Figures 23(**f**)-23(**h**) then show the formation of low angle bands from these melt-enriched regions. These bands are oriented at $15 - 20^\circ$ to the shear plane, and so are consistent with the results from section 4. Eventually, in Figure 23(**i**), we see that the bands that form tangentially to the inclusion become detached, leaving a melt-depleted region around the inclusion.

These results bear particular resembelance to the images from experiments [1], where we see the porosity bands forming away from the inclusion. These appears to occur for large strains, which again is consistent with the large strains in these experiments.

As a further test we perform the same simulations, however this with less diffusion. To do this we take a larger value of m, and we chose $m = 4$. Other parameter values for this simulations are identical to the previous run. Again, the formation of low angle porosity bands is prevalent. The reduction of the diffusion in the model also seems to permit the growth of separate bands that are further away from the inclusion. For example, Figure 24 shows evidence of other porosity bands forming nearer to the top and bottom boundaries. Interestingly, there also appears to be some band reconnection occuring in Figures 24(**i**)-24(**k**). A seperate band forms off the band placed to the right of the inclusion, and growth seems to be favoured in the band to the left of the inclusion.

In conclusion, we can see that with the addition of anisotropic viscosity, and diffusion, we can see the formation and growth of low-angle bands, tangential to the inclusion. A future extension of this work would be to incorporate dynamic anisotropy into the code.

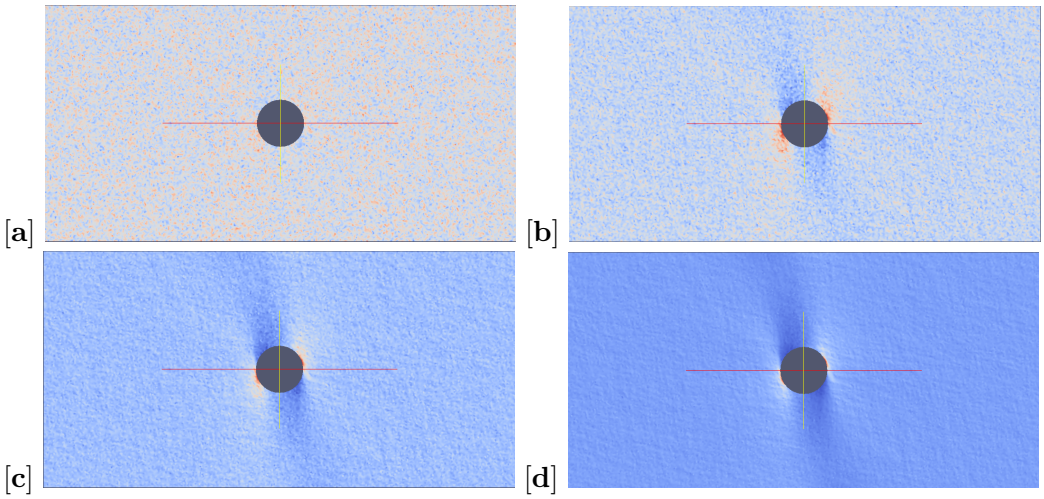

Figure 22: *Snapshots from simulation of the flow around inclusion with anisotropic viscosity,* $\alpha = 2$ *and* $\Theta = \pi/4$*. There is no diffusion in this model. The time-step was taken to be* $\Delta t = 5 \times 10^{-3}$*, with a mesh resolution of* $400(i) * 200(j)$ *grid cells. Other parameters are taken to be* $R = 1$*,* $\lambda = -27$*,* $\tau_\xi = 5/3$*, and* $\phi_0 = 0.05$*, and the amplitude of the background noise perturbation is* $\epsilon = 10^{-3}$*. (**a**)-(**d**) show the porosity profile at* $T = 0$*,* $5\Delta t$*,* $10\Delta t$ *and* $20\Delta t$ *time-steps, respectively.*

8 Conclusion

We briefly conclude the work presented in this report. One of the main outcomes of this work is preliminary indication of the capability of GST to complement previous analysis. This is seen in the GST calculations that reproduced melt-localised bands in a variety of different flow configurations; such as for simple shear and 2-D Poiseuille flow. It is also able to identify a low angle banded instability for the a model which includes viscous anisotropy [23]. In addition to identify optimally growing perturbations to some initial state, there is some suggestion that GST can be used to highlight secondary instabilities.

We were able to go further and use GST to predict optimally growing perturbations for the problem of a compactable two-phase flow around a cylindrical inclusion, as motivated by experiments [1]. These GST calculations were able to identify a banded instability to the porosity field, in regions adjacent to the cylinder. The extension of the code to simulate the inclusion problem produces results that fit more closely with the experiments. In our results we see porosity bands forming tangentially to the inclusion boundary, and then eventually moving off the boundary. Further, as shown in Figures 23 and 24, these bands form at low angles $(15 - 20^\circ)$ when we include anisotropic viscosity. This also appears to be consistent with recent experiments. To our knowledge, this is the first time this ype of behaviour has been documented in simulations.

The final conclude by stressing that although GST can be used higlight important features of the system in equations (34)-(36), in a variety differnet flow configurations, it is still undecided what its most useful function is. With time, it is hoped that the application of GST will evolve to become an even more important, integral tool in studying magma/mantle dynamics, as new and interesting questions arise.

References

[1] Y.-H Zhao C. Qi and D. L. Kohlstedt. An experimental study of pressure shadows in partially molten rocks. *Earth Plan. Sci. Lett.*, 2013. Submitted.

[2] B. F. Farrell and P. J. Ioannou. Generalized stability theory. part i: Autonomous operators. *Journal of the Atmospheric Sciences*, 53:20252040, 1996.

[3] B. F. Farrell and P. J. Ioannou. Generalized stability theory. part ii: Nonautonomous operators. *Journal of the Atmospheric Sciences*, 53:20412053, 1996.

[4] P.E. Farrell and S.W. Funke. Exploiting high-level structure in algorithmic differentiation. 2013. Submitted.

[5] B.K. Holtzman, N.J. Groebner, M.E. Zimmerman, S.B. Ginsberg, and D.L. Kohlstedt. Stress-driven melt segregation in partially molten rocks. *Geochem. Geophys. Geosys.*, 4, 2003.

[6] B.K. Holtzman and D.L. Kohlstedt. Stress-driven melt segregation and strain partitioning in partially molten rocks: Effects of stress and strain. *J. Petrol.*, 48:2379–2406, 2007.

[7] R.F. Katz, M. Spiegelman, and B. Holtzman. The dynamics of melt and shear localization in partially molten aggregates. *Nature*, 442, 2006.

[8] Richard F Katz and Yasuko Takei. Consequences of viscous anisotropy in a deforming, two-phase aggregate: 2. Numerical solutions of the full equations. *J. Fluid Mech.*, 2012. Submitted.

[9] Anders Logg, Kent-Andre Mardal, Garth N. Wells, et al. *Automated Solution of Differential Equations by the Finite Element Method*. Springer, 2012.

[10] A. M. Lyapunov. *The General Problem of the Stability of Motion, Control Theory and Applications Series*. Taylor Francis, 1892.

[11] D. McKenzie. The generation and compaction of partially molten rock. *J. Petrol.*, 25, 1984.

[12] D. McKenzie and M. Holness. Local deformation in compacting flows: development of pressure shadows. *Earth Plan. Sci. Lett.*, 2000.

[13] S. W. Funke P. E. Farrell, D. A. Ham and M. E. Rognes. Automated derivation of the adjoint of high-level transient finite element programs. 2012.

[14] C.J. Cotter P.E. Farrell and S.W. Funke. A framework for the automation of generalised stability theory. 2012.

[15] J. Rudge. Compaction around a rigid sphere: analytical solutions. *J. Fluid Mech.*, 2013. In preparation.

[16] P. J. Schmid. Nonmodal stability theory. *Annual Review of Fluid Mechanics*, 39:129–162, 2007.

[17] D.R. Scott and D.J. Stevenson. Magma ascent by porous flow. *J. Geophys. Res.*, 91, 1986.

[18] M. Spiegelman. Flow in deformable porous-media. part 1. Simple analysis. *J. Fluid Mech.*, 247, 1993.

[19] M. Spiegelman. Linear analysis of melt band formation by simple shear. *Geochem. Geophys. Geosys.*, 2003.

[20] D.J. Stevenson. Spontaneous small-scale melt segregation in partial melts undergoing deformation. *Geophys. Res. Letts.*, 16, 1989.

[21] Y. Takei and B.K. Holtzman. Viscous constitutive relations of solid-liquid composites in terms of grain boundary contiguity: 1. Grain boundary diffusion control model. *J. Geophys. Res.*, 2009.

[22] Y. Takei and B.K. Holtzman. Viscous constitutive relations of solid-liquid composites in terms of grain boundary contiguity: 2. Compositional model for small melt fractions. *J. Geophys. Res.*, 2009.

[23] Yasuko Takei and Richard F Katz. Consequences of viscous anisotropy in a deforming, two-phase aggregate: 1. Governing equations and linearised analysis. *J. Fluid Mech.*, 2013.

[24] ME Zimmerman, SQ Zhang, DL Kohlstedt, and S Karato. Melt distribution in mantle rocks deformed in shear. *Geophys. Res. Letts.*, 26(10):1505–1508, 1999.

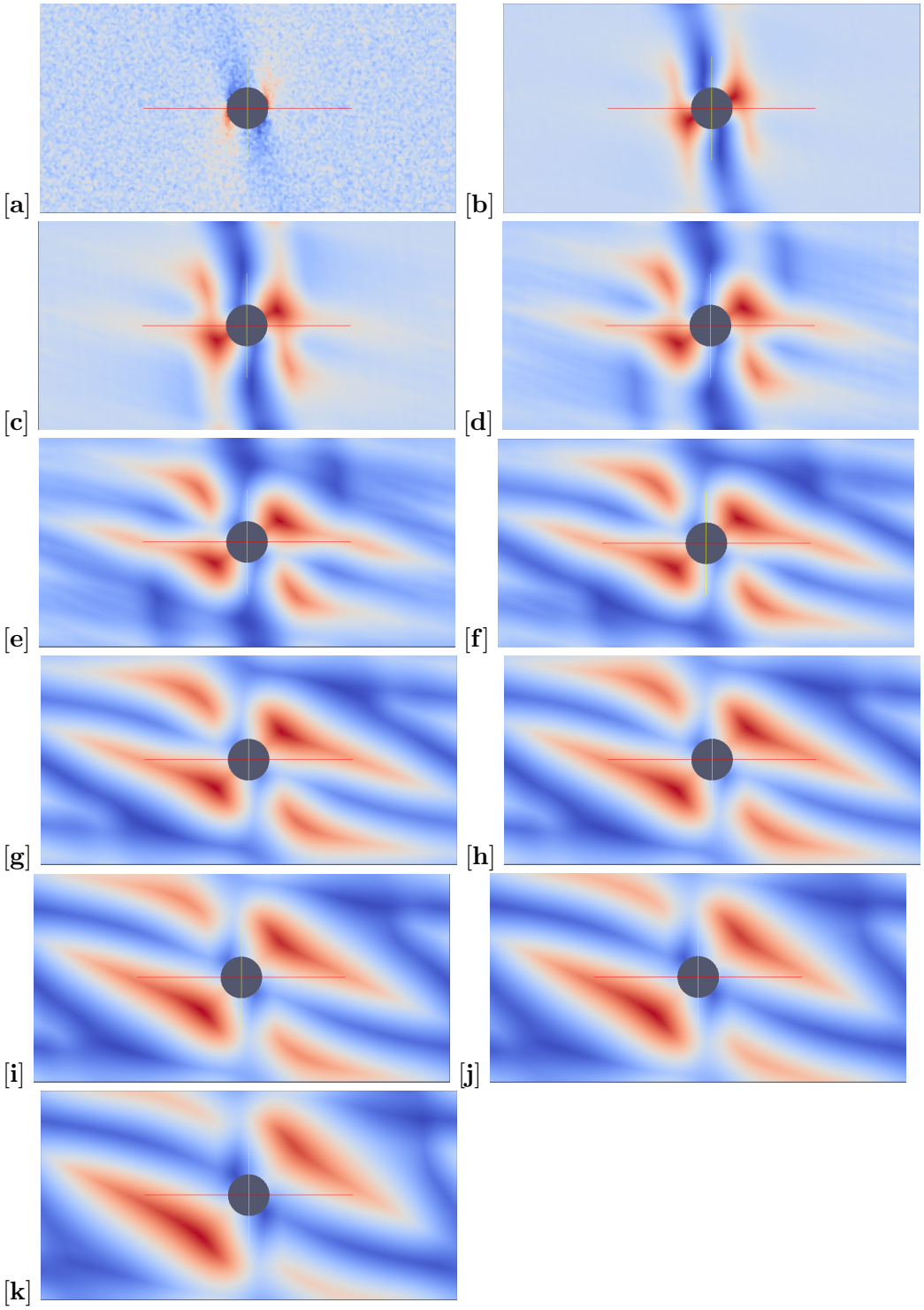

Figure 23: *Snapshots from simulation of the flow around inclusion with anisotropic viscosity. The parameter regime is the same except that diffusion is included in this model, with a diffusion exponent* $m = 3$. *(**a**) shows the initial porosity profile at* $T = 0$, *and the (**b**)-(**k**) show the evolved porosity at intervals of* $50\Delta t$. *(**k**) shows the final state at* $T = 500\Delta t$, *and the maximum porosity is 0.158.*

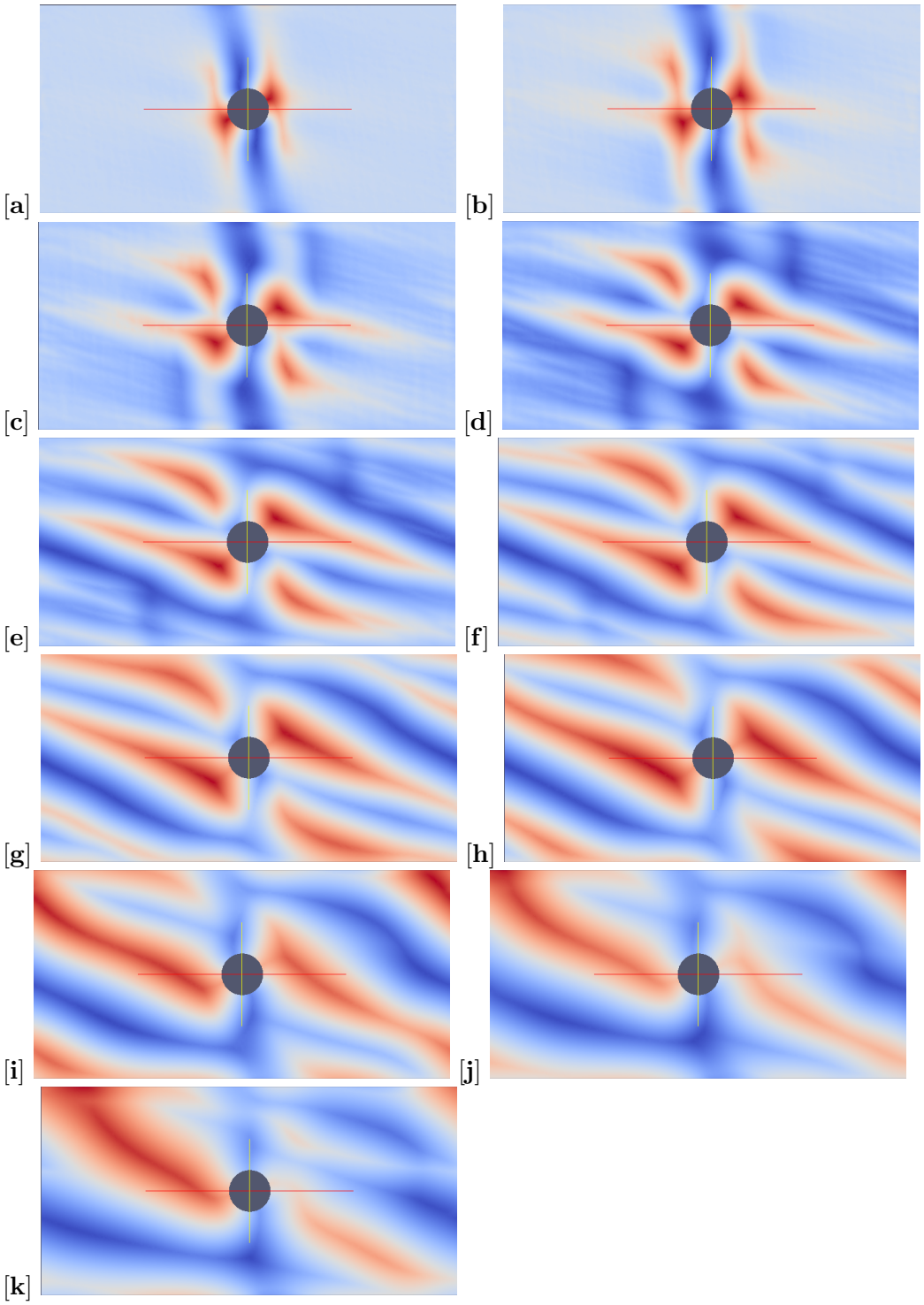

Figure 24: *Same simulation but this time with less diffusion. This is done by taking* $m = 4$. ***(a)*** *shows the porosity profile at* $T = 50\Delta t$*, and the* ***(b)-(f)*** *show the evolved porosity at intervals of* $50\Delta t$*.* ***(k)*** *shows the porosity profile state at* $T = 300\Delta t$*.* ***(g)-(k)*** *shows the further evolution at intervals of* $100\Delta t$*.* ***(k)*** *shows the final state at* $T = 800\Delta t$*, and the maximum porosity is 0.209.*